nature communications

Article

https://doi.org/10.1038/s41467-025-61041-4

Two-dimensional superlattice nanocatalysts unlock multimodal energy transformation-driven catalytic therapy

Received: 17 October 2024

Accepted: 11 June 2025

Published online: 01 July 2025

Check for updates

Shanshan Zhang[1,7], Xiangyu Kong[1,7], Ximo Xu[2], Qing Hua[1], Wenwen Xu[1], Liang Chen[3,4] ✉, Jianqiao Zhou[1,5] ✉ & Yu Chen[3,6] ✉

While the development of nanochemistry has spurred the emergence of catalytic nanomedicine, nanocatalysts with multifaceted catalytic properties for therapeutic applications remain underexplored. Here, we present two-dimensional BiCuSeO nanosheets (BCSO NSs) as the superlattice nanocatalyst for multimodal energy transformation-driven nanocatalytic therapy. Benefiting from the intrinsic layered heterostructures and a narrow bandgap, BCSO NSs feature photothermoelectric and sono-piezoelectric catalytic effects, as well as enzyme-mimicking catalytic activities. Theoretical calculations reveal that the internal electric fields within superlattice nanostructures contribute to the rapid separation and suppressed recombination of charge carriers. Consequently, BCSO NSs enable controlled reactive oxygen species generation under the second near-infrared light or ultrasound irradiations. The enzymatic activity of BCSO NSs also facilitates the transformation of tumor-specific substrates, dysregulating the redox homeostasis. The photothermoelectric and sono-piezoelectric/enzymatic activities of BCSO NSs have been exemplified by antibacterial and anticancer applications, highlighting the potential of two-dimensional superlattice nanocatalysts to address diverse pathological abnormalities.

The rapid advancement of nanotechnology and nanomedicine over the past decade has substantially driven the exploration of diverse nanocatalysts in biomedicine[1–5]. These nanocatalysts can mediate the transformation of specific substances to generate highly toxic reactive oxygen species (ROS) for efficient treatments against pathological abnormalities such as cancer and bacterial infections[6–9]. However, the efficacy of nanocatalytic therapy is often counteracted by the low concentration of endogenous H_2O_2 (50-100 μM) and the high level of reducing substances such as glutathione (GSH)[10–13]. These limitations necessitate the exploration of distinctive catalytic modalities to improve their clinical application potential[14,15]. Recently, nanocatalysts with energy transformation capabilities have attracted increasing research interest at the intersection of catalysis and nanomedicine[16,17]. Piezoelectric catalysis represents an emerging modality for energy transformation-mediated catalytic therapy[18–20]. Specifically, when externally activated by mechanical energy such as ultrasound (US) irradiation, sono-piezoelectric nanocatalysts spontaneously generate a piezoelectric potential that drives charge separation or transfer, thereby triggering ROS generation via surface redox reactions for therapeutic purposes[21]. In this cascade of mechanical-to-electrical-to-

[1]Department of Ultrasound, Ruijin Hospital, Shanghai Jiaotong University School of Medicine, Shanghai 200025, P. R. China. [2]Department of General Surgery, Shanghai General Hospital, Shanghai Jiaotong University School of Medicine, Shanghai 200080, P. R. China. [3]Materdicine Lab, School of Life Sciences, Shanghai University, Shanghai 200444, P. R. China. [4]State Key Laboratory of Molecular Engineering of Polymers, Fudan University, Shanghai 200438, P. R. China. [5]College of Health Science and Technology, Shanghai Jiaotong University School of Medicine, Shanghai 200025, P. R. China. [6]Shanghai Institute of Materdicine, Shanghai 200052, P. R. China. [7]These authors contributed equally: Shanshan Zhang, Xiangyu Kong. ✉e-mail: liangchenbio@shu.edu.cn; zjq11432@rjh.com.cn; chenyuedu@shu.edu.cn

chemical energy transformation, US with a high tissue-penetration depth serves as the only input energy to control the output of chemical energy spatiotemporally. Photothermoelectric (PTE) catalysis is another cutting-edge catalytic mode for biomedical applications[22]. Unlike thermoelectric catalysis, which requires temperature fluctuations as a trigger, PTE materials generate thermal energy upon light illumination, enabling more efficient photonic-to-thermal-to-electric-chemical energy transformation through combined photothermal and thermoelectric effects[23]. Furthermore, in contrast to photocatalytic processes where the rapid recombination of photogenerated electrons and holes constrains the production of ROS, the PTE can directly leverage photonic energy-mediated thermal fluctuations to induce thermoelectric potentials[24–26]. The established built-in electric field can delay charge recombination, ensuring high ROS generation and catalytic activity[27]. Consequently, PTE presents extensive potential for applications in the biomedical field. Despite their great potential, sono-piezoelectric and PTE catalytic therapy are still in their infancy, with several weaknesses yet to be addressed. Most currently developed piezoelectric and thermoelectric nanocatalysts exhibit unsatisfactory ROS yields, primarily due to their lower energy-harvesting capacities and limited functional capabilities. Additionally, the complexity of the tumor microenvironment poses significant challenges for single-mode catalytic therapy in achieving complete tumor eradication[28]. Therefore, there is an urgent need to explore exceptional nanocatalysts with multimodal energy transformation capabilities and synergistically coordinated endogenous and exogenous catalytic effects.

From the materials science perspective, the construction of heterojunctions is widely recognized as one of the most effective and practical strategies for integrating multiple catalytic modes and enhancing overall catalytic efficiency. For instance, barium titanate (BTO) is well known for its intrinsic thermoelectric and piezoelectric properties. While BTO has been extensively explored for sono-piezoelectric catalytic therapy, its thermoelectric potential remains largely underutilized in biomedical applications[29,30]. This limitation primarily stems from the fact that pristine BTO lacks intrinsic photothermal conversion capability, preventing effective thermoelectric activation under external stimuli. To overcome this, researchers have integrated photothermal conversion agents with BTO, enabling synergistic thermoelectric catalytic applications[31,32]. Moreover, researchers have synthesized hybrid transition metal dichalcogenides with phase junctions to synergize PTE effects with multienzyme activities[22]. Two-dimensional (2D) heterostructures with unique 2D/2D face-to-face contacted interfaces typically feature higher charge mobility and lower charge recombination rates than other geometries[33,34]. Particularly, 2D superlattice nanosheets, composed of alternately restacked 2D unilamellar nanosheets at the molecular scale, offer exceptional flexibility in fully exploiting the unique properties of distinct atomic layers for catalytic applications[35]. Nevertheless, the practical application of 2D superlattices remains hampered by the complexity of synthetic procedures and the lack of precise control over nanoscale lateral dimensions[36]. On the other hand, the sono-piezoelectric and PTE effects of 2D superlattices have not been explored. To fill this gap, it is highly desirable to develop 2D superlattice nanocatalysts that not only can be fabricated by facile routes but also possess suitable bandgap and multifaceted catalytic properties for energy transformation-mediated nanocatalytic therapy.

Here, we propose that BiCuSeO nanosheets (BCSO NSs), a natural superlattice with alternating stacks of metal selenides $[Cu_2Se_2]^{2-}$ and metal oxides $[Bi_2O_2]^{2+}$ sublayers[37,38], serve as a versatile nanocatalyst with multimodal energy transformation capabilities for nanocatalytic applications in biomedicine. Specifically, the BCSO NSs are prepared by a facile hydrothermal method (Fig. 1a). Taking advantage of their innate heterostructures and narrow bandgap[39], these superlattice nanosheets enable multimodal energy transformation-driven ROS generation upon exogenous or endogenous energy inputs (Fig. 1b). First, under the second near-infrared (NIR-II) photonic illumination (1064 nm), BCSO NSs can exert PTE effects to facilitate photonic-thermal-electric-chemical energy transformation for photo-initiated ROS generation. Simultaneously, the NIR-II photothermal conversion ability of BCSO NSs mediates the output of photoacoustic (PA) signals through photonic-thermal-acoustic energy transformation. In addition, BCSO NSs show exceptional piezoelectric effects that convert the inputted mechanical energy to electrical energy and subsequently to chemical energy, thereby generating ROS through US-mediated sono-piezoelectric catalysis. The inclusion of transition metal elements in their compositions also endows BCSO NSs with enzyme-like activity, showcasing an energy transformation mode of chemical catalytic reactions. Density functional theory (DFT) calculations reveal the built-in electric field within intrinsic heterostructure and the narrow bandgaps of superlattice NSs, which facilitates the spontaneous separation and rapid migration of charge carriers under exogenous energy activation. COMSOL multiphysics simulations further provide a detailed view of the potential distribution on the BCSO NSs.

Benefiting from their multifaceted catalytic mechanisms, BCSO NSs are highly adaptable to diverse biomedical scenarios (Fig. 1c and d). As a proof of concept, NIR-II light-mediated PTE catalytic antibacterial application of BCSO NSs was exemplified by a superficial wound infection model. Moreover, the sono-piezoelectric effect and peroxidase (POD)-like enzymatic activity of BCSO NSs were harnessed to precisely target and eradicate tumors. Upon the input of mechanical US energy, the elevated ROS generation, coupled with the tumor-specific GSH depletion by BCSO NSs, can effectively dysregulate the intracellular redox homeostasis, inducing ferroptosis and apoptosis in cancer cells and thereby enhancing the nanocatalytic therapeutic efficacy. Given that such multimodal energy transformation capabilities have not been previously demonstrated in other materials, to the best of our knowledge (Table S1 and S2), this study presents a paradigm of superlattice nanocatalysts with photothermoelectric/sono-piezoelectric/enzymatic catalytic effects for versatile biomedical applications.

Results

Preparation and characterization of superlattice BCSO nanocatalysts

The superlattice BCSO NSs were fabricated via a mild hydrothermal route. Transmission electron microscopy (TEM) images revealed that the synthesized BCSO NSs exhibited a uniform sheet-like morphology. The average length and width of the BCSO NSs were measured to be 85.56 nm and 63.28 nm (Fig. 2a and supplementary Fig. 2), respectively. Dynamic light scattering (DLS) measurements showed an average hydrodynamic diameter of ~212.2 nm (Fig. 2a), which is relatively larger due to the irregular shape of NSs and the existence of a hydration shell on the surface. AFM characterization revealed the 2D nanosheet morphology of BCSO NSs with a thickness of ~13.65 nm (about 15 layers) (Supplementary Fig. 2). Moreover, favorable colloidal stability of modified BCSO NSs was observed over 7 days in biological environments (Supplementary Fig. 3), which is beneficial for their biomedical applications. Zeta potential results demonstrated the negative surface charge of modified BCSO NSs, offering advantages for their in vivo pharmacokinetics within the biological system (Supplementary Fig. 4). The high-resolution TEM (HRTEM) image distinctly revealed two sets of mutually perpendicular lattice fringes, each with a spacing of ~0.28 nm (Fig. 2b)[40]. These lattice fringes are attributed to the (110) and (1-10) planes of tetragonal BCSO NSs[39]. Additionally, a single set of diffraction spots displaying fourfold symmetry was observed in the selected area electron diffraction (SAED) pattern (Fig. 2c), demonstrating high crystallographic orientation along the c-axis of the synthesized superlattice NSs. This is in agreement with the findings from HRTEM observation. Elemental mapping analysis (Fig. 2d) confirmed the homogeneous distribution of all expected

https://doi.org/10.1038/s41467-025-61041-4

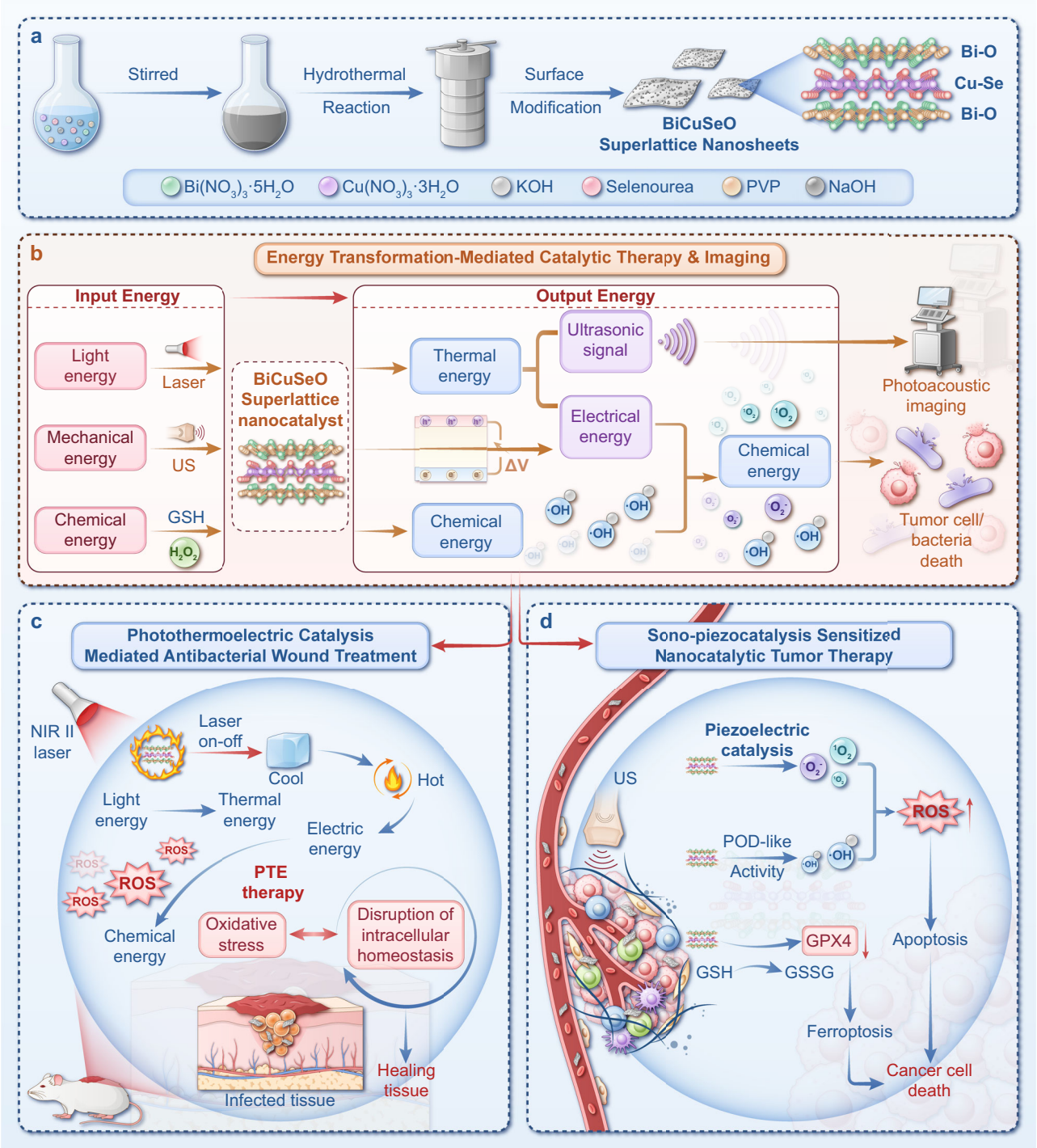

Fig. 1 | Schematic illustration for the preparation and therapeutic application of BCSO NSs. a Schematic illustration of the synthesis process for BCSO NSs. **b** Schematic illustration of the multifaceted energy conversion effects based on superlattice 2D BCSO nanocatalysts for theranostic applications. **c** BCSO NSs-mediated PTE catalytic therapy effectively generates abundant ROS, disrupting the intracellular homeostasis within bacteria for non-invasive treatment of wound infections. **d** Sono-piezocatalysis enhanced nanocatalytic therapy induces apoptosis and synergistic ferroptosis in melanoma cells, thereby significantly improving antitumor efficacy.

elements throughout the 2D lamellar structures. Furthermore, the powder X-ray diffraction (PXRD) peaks of BCSO NSs matched well with the standard diffraction card (PDF#46-0296) (Fig. 2e), indicating the high purity and crystallinity of the synthesized NSs[41].

As BCSO NSs are theoretically characterized by a layered superlattice nanostructure composed of periodically stacked conductive $[Cu_2Se_2]^{2-}$ and insulating $[Bi_2O_2]^{2+}$ sublayers (Fig. 2f), their atomic arrangement was further elucidated through HRTEM observation. Lattice images along the [001] zone axis (c-axis) displayed a highly ordered distribution of Bi atoms, and their corresponding fast Fourier transform (FFT) image exhibited no spot splitting (Fig. 2g). These findings indicate that the two sublattices (Cu-Se and Bi-O) are commensurate along the c-axis. Moreover, images along the [100] zone axis revealed a periodically stacked layered structure, in which each layer was marked by distinct atomic spots (Fig. 2h). Notably, splitting phenomena can be observed in the FFT image. Furthermore, the

https://doi.org/10.1038/s41467-025-61041-4

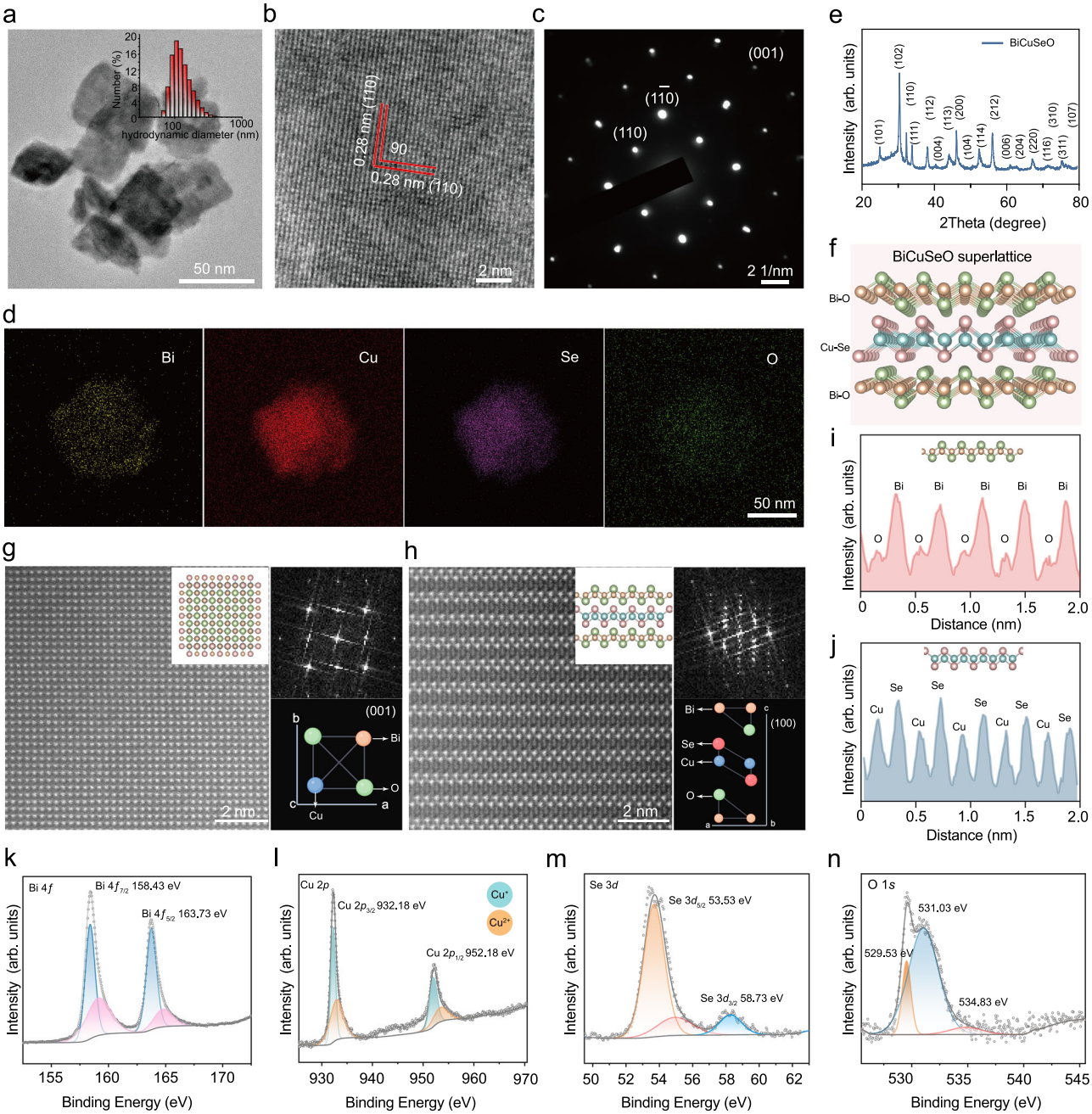

Fig. 2 | Structure and composition characterization of BCSO NSs. a TEM images of BCSO NSs. The inset indicates the hydrodynamic size distribution of BCSO NSs. **b** HRTEM image of lattice fringes. **c** Corresponding SAED pattern of superlattice BCSO NSs. **d** EDS mapping images and (**e**) XRD pattern of BCSO NSs. **f** Structural model of BCSO NSs. HRTEM images accompanied by the corresponding FFT patterns, and schematic representations of the atomic distribution of BCSO NSs oriented along (**g**) [001] and (**h**) [010] zone axes, respectively. The spatial arrangement of atoms within the (**i**) Bi-O and the (**j**) Cu-Se layers along the [010] zone axes. **k** Bi 4 f, (**l**) Cu 2p, (**m**) Se 3 d and (**n**) O 1 s XPS spectra for BCSO NSs. Source data are provided as a Source Data file.

regularly arranged Bi, Cu, Se, and O atoms within the Bi-O and Cu-Se layers can be identified through the intensity line profiles (Fig. 2i, j). High-resolution X-ray photoelectron spectroscopy (XPS) was performed to investigate the elemental compositions and chemical states. Initially, the total XPS spectrum revealed the atomic ratio of BiCuSeO NSs to be Bi:Cu:Se:O = 1:1.32:1.86:1.06 (Supplementary Fig. 5). As expected, the surveyed Bi 4*f* core-level spectrum of BCSO NSs confirmed the emergence of oxidation state Bi (Fig. 2k). Meanwhile, in the Cu 2*p* XPS spectrum, two distinct peaks at binding energies of 952.18 eV and 932.18 eV corresponded to the Cu $2p_{1/2}$ and Cu $2p_{3/2}$ states, respectively, suggesting the coexistence of Cu^{+} and Cu^{2+} (Fig. 2l). Two typical Se 3*d* characteristic peaks can be found at the binding energies of 54.07 eV and 58.64 eV (Fig. 2m). The O 1*s* XPS spectrum of BCSO was deconvoluted into three peaks, where the peaks at 529.53 eV and 531.03 eV were assigned to Bi-O and Bi-OH bonds, respectively. A prominent peak at 534.29 eV with higher binding energy is likely attributable to carbonate substances adsorbed on the surface (Fig. 2n)[42,43]. These structural characterization results collectively corroborate the successful synthesis of 2D superlattice BCSO nanocatalysts.

PTE energy transformation-mediated catalytic performance of superlattice BCSO NSs

Building on the thermoelectric effects of BCSO-based materials, we aim to explore their potential as PTE catalysts for thermal-electric-chemical energy transformation in biomedical applications. First, the temperature-dependent electrical conductivity (σ), Seebeck coefficient (*S*), and thermal conductivity (κ) of BCSO NSs were measured to calculate the corresponding merit ZT values within a temperature range of 300-550 K (Supplementary Fig. 6). The *S* values of BCSO NSs increased with temperature, and their *S* values were positive. This suggests that these nanocatalysts possess the properties of p-type degenerate semiconductors, with charge transport predominantly facilitated by holes[39]. Furthermore, the κ of BCSO NSs decreased with an increase in temperature. The dimensionless Fig. of merit (ZT) values can be calculated by the formula below:

$$ZT = S^2\sigma T/\kappa \quad (1)$$

Accordingly, a gradual increase in ZT values with elevated temperatures was observed. These findings indicate that the synthesized superlattice BCSO NSs feature both electrical and thermal transport capabilities in response to temperature variations. Therefore, it is expected that temperature fluctuation cycles can activate BCSO NSs to facilitate the formation of a built-in electric field for thermoelectric catalysis. Furthermore, owing to their strong inherent NIR-II absorption, BCSO NSs can responsively generate thermal gradients upon an on/off cycle irradiation of a 1064 nm laser, thereby enabling PTE-triggered ROS generation (Fig. 3a). Accordingly, the thermoelectric catalytic performance of BCSO NSs was first evaluated under manual thermal gradients using 1,3-diphenylisobenzofuran (DPBF) as a singlet oxygen ($^1O_2$) probe. When the BCSO NSs were alternately incubated at 30 °C and 45 °C, a significant decrease in the characteristic absorption peak of DPBF was observed (Fig. 3b, Supplementary Fig. 7). After five cycles, the absorbance of the BCSO NSs solution containing DPBF at its characteristic peak dropped by 53.74% (Fig. 3c), indicating thermoelectric-mediated ROS production under manual thermal gradients. The fluorescence of 9,10-anthracenediyl-bis(methylene)dimalonic acid (ABDA) also continually decreased after a temperature gradient was applied to BCSO NSs, similarly confirming the generation of $^1O_2$ during the thermoelectric catalytic process (Supplementary Fig. 8a**)**. Additionally, the nitroblue tetrazolium (NBT) probe was used to detect the generation of superoxide anions ($\cdot O_2^-$) during the thermoelectric process. The characteristic absorption peak of NBT at 260 nm decreased with an increasing number of thermal cycles, confirming the production of$\cdot O_2^-$ (Supplementary Fig. 9). Dihydroethidium (DHE), a fluorescent probe that can be oxidized by $\cdot O_2^-$ to produce ethidium, was also employed to verify this. Consistently, the fluorescence intensity of ethidium increased by 32.50% compared to the control group after thermal cycling (Supplementary Fig. 10a). These results collectively demonstrate the thermoelectric catalytic properties of BCSO NSs to produce both $\cdot O_2^-$ and $^1O_2$.

Subsequently, the NIR-II photothermal performance of BCSO NSs was assessed before investigating their PTE catalytic efficacy. As expected, upon NIR-II irradiation, the temperature of the BiCuSeO suspension rapidly increased in both concentration-dependent and laser power density-dependent manners (Fig. 3d, Supplementary Figs. 11 and 12). Additionally, the high photostability of superlattice NSs was validated by consistent thermal energy output under repeated NIR-II irradiation (Supplementary Fig. 13). The photothermal conversion efficiency (η) of BCSO NSs at 1064 nm was calculated to be ~31.6% (Fig. 3e, Supplementary Fig. 14). To further investigate the underlying mechanism of PTE effects of BCSO NSs, electrochemical impedance spectroscopy (EIS) Nyquist plots were recorded both with and without 1064 nm laser irradiation. The data revealed a significant reduction in the semicircle radius of BCSO NSs upon NIR-II illumination (Supplementary Fig. 15a), suggesting that photon energy input drives the photothermoelectric (PTE) effect, resulting in decreased impedance and enhanced electron transfer in BCSO NSs. Furthermore, the transient temperature increases and decreases caused by the NIR-II laser on/off cycles could induce sharp rises or falls in current density, as evidenced by the photocurrent curve of BCSO NSs (Supplementary Fig. 15b). In contrast, the current density gradually decreased once the laser was turned off, which is presumably attributed to the charge redistribution in the absence of the PTE effect. These results confirm that BCSO NSs can efficiently generate charge carriers under NIR-II photonic activation.

Next, the PTE-mediated $^1O_2$ generation capability of BCSO NSs was evaluated. We irradiated BCSO NSs with a 1064 nm laser (laser on), followed by natural cooling to room temperature (laser off). The characteristic absorption peak of DPBF progressively declined with increasing cycle numbers (Supplementary Fig. 16). Quantitative analysis further demonstrated the high efficiency of BCSO NSs in generating $^1O_2$ under laser-controlled temperature fluctuation (Fig. 3f). Similarly, the fluorescence of ABDA significantly decreased after photothermal cycling, further confirming the generation of $^1O_2$ during the PTE process (Supplementary Fig. 8b). Following photothermal-induced thermal cycling, there was a decrease in the characteristic absorption peak of NBT at 260 nm, accompanied by a 32.68% increase in DHE fluorescence relative to the control, indicating the production of $\cdot O_2^-$ (Supplementary Figs. 17 and 10b). Electron spin resonance (ESR) spectra also showed the characteristic peaks corresponding to $^1O_2$ species and $\cdot O_2^-$ for BCSO NSs upon thermal cycle or on/off cycles of NIR-II irradiation (Fig. 3g, h). Collectively, those evidence validates the effectiveness of superlattice BCSO NSs as an energy transformation-based nanocatalyst for PTE catalytic therapy.

Sono-piezoelectric/enzymatic catalytic effects of superlattice BCSO NSs

While the thermoelectric effect of BCSO NSs has been widely studied in chemical catalysis, their piezoelectric effect remains unexplored. Thus, we aimed to evaluate the potential of BCSO NSs as sono-piezoelectric nanocatalysts by employing the US as the mechanical trigger. First, piezoresponse force microscopy (PFM) was employed to inspect the piezoelectric properties of BCSO NSs. The phase image of BCSO NSs demonstrated significant piezoelectric behavior (Supplementary Fig. 18). Under continuous voltage stimulation, the amplitude changes of BCSO NSs exhibited a butterfly curve, indicative of varying strain. Meanwhile, a 180° phase shift was recorded as a hysteresis loop, demonstrating the piezoelectric properties of BCSO NSs (Fig. 3i)[44]. The bandgap of the superlattice BCSO NSs was measured to be 1.04 eV based on the UV-vis diffuse reflectance spectrum (Supplementary Fig. 19a). Such a narrow bandgap facilitates the separation of electron-hole pairs under US irradiation[38]. The generated electrons and holes can participate in the piezoelectric redox reactions at the conductive band (CB) and valence band (VB), respectively[20,45]. Therefore, the sono-piezoelectric catalytic performance of BCSO NSs was evaluated. Unsurprisingly, the characteristic absorption peak of the DPBF solution containing BCSO NSs gradually decreased with the prolonged US irradiation time, signifying the continuous production of $^1O_2$ (Fig. 3j, Supplementary Fig. 20). Moreover, the ability of BCSO NSs to generate $\cdot O_2^-$ via piezocatalytic activity under US stimulation was assessed using the NBT probe. Similarly, the generation of $\cdot O_2^-$ was corroborated by the downtrend in the characteristic absorption peak of NBT at around 260 nm (Fig. 3k, Supplementary Fig. 21). ABDA and DHE were also utilized to respectively ascertain the production of $^1O_2$ and $\cdot O_2^-$ during the sono-electric catalytic process (Supplementary Figs. 8c and 10c). The ROS generation was further validated by ESR spectra analysis, which revealed typical $^1O_2$ and $\cdot O_2^-$ signals with corresponding characteristic peaks presented in the BCSO + US group (Fig. 3l, m).

https://doi.org/10.1038/s41467-025-61041-4

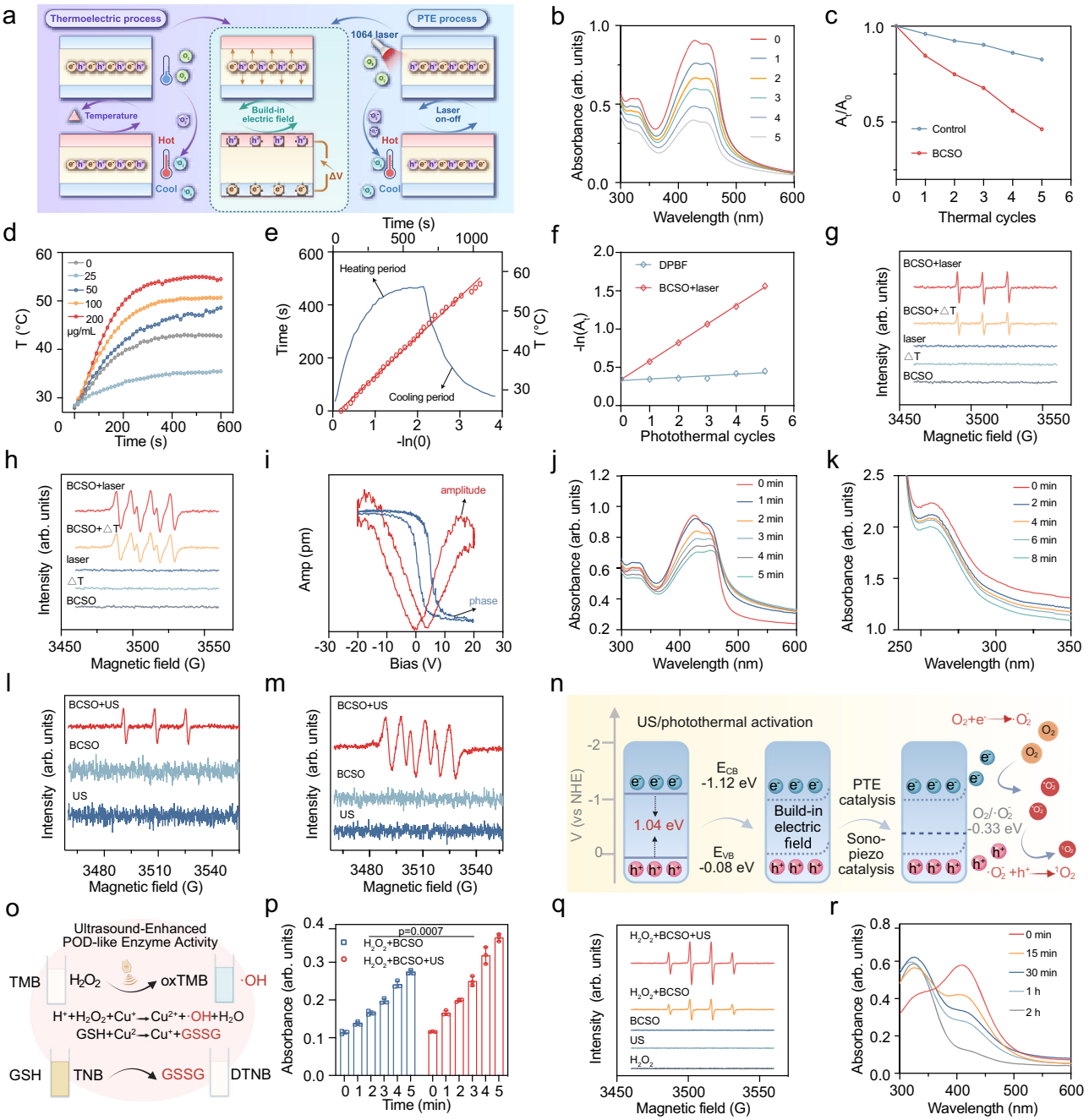

Fig. 3 | Multimodal energy conversion catalytic effects of superlattice BCSO nanocatalysts. a Schematic illustration of the thermoelectric and PTE catalysis process. **b** UV-vis absorption spectra of DPBF solutions incubated with BCSO NSs during five heating/cooling cycles. **c** Thermal cycles-dependent $^1O_2$ production reflected by the decline in peak absorbance of DPBF. **d** Photothermal curves of superlattice BCSO nanocatalysts at different concentrations under laser irradiation. **e** Heating/cooling curves of BCSO NSs upon exposure to laser irradiation and linear time constant calculated from the cooling period. **f** Regression analysis of DPBF oxidation efficiency of BCSO NSs under laser irradiation for 5 cycles. **g** ESR spectra in different groups using TEMP as the $^1O_2$ capture agent, including control, BCSO NSs, and BCSO NSs after being exposed to temperature gradient or alternating laser irradiation. **h** ESR results demonstrate BCSO NSs generated $\cdot O_2^-$ under temperature gradients or photothermal cycles. **i** The amplitude image (red) and phase image (blue) of BCSO NSs observed by PFM. **j** UV–vis spectra of DPBF solution containing BCSO NSs under US irradiation for different durations. **k** $\cdot O_2^-$ generation from the BCSO NSs under US irradiation characterized by NBT. ESR results indicate (**l**) $^1O_2$ and (**m**) $\cdot O_2^-$ generation by BCSO NSs after being exposed to US irradiation. **n** Schematic diagram of the bandgap analysis of BCSO NSs and its catalytic mechanism under ultrasonic/photothermal activation (Created with BioRender.com). **o** Mechanistic diagram of multiple enzyme activities of BCSO NSs. **p** Time-course absorbance change of TMB in the presence of BCSO NSs with or without US irradiation ($n = 3$ independent samples, mean ± SD, two-way ANOVA). **q** ESR spectra in different groups using DMPO as the ·OH capture agent. **r** Time-dependent GSH depletion by BCSO NSs. Source data are provided as a Source Data file.

Additionally, superoxide dismutase (SOD) and β-carotene were used to selectively scavenge $\cdot O_2^-$ and $^1O_2$, respectively. ESR spectra demonstrated a notable decrease in characteristic signal peaks following the introduction of these scavengers, further confirming the generation of various types of ROS (Supplementary Fig. 22a, b). These data demonstrate that the sono-generated electrons can efficiently catalyze the oxygen reduction reactions to generate cytotoxic ROS.

Inspired by the bifunctional PTE and sono-piezoelectric catalytic properties of BCSO superlattice NSs, we investigated their potential synergistic effects by sequentially exposing them to NIR laser and US

irradiation. The results revealed a more pronounced decrease in the characteristic ABDA peak at 375 nm compared to single-mode PTE or sono-piezoelectric catalysis, indicating enhanced $^1O_2$ generation under combined catalytic activation (Supplementary Fig. 8d). Furthermore, the ethidium fluorescence intensity increased by 41.83% in the combination group, significantly surpassing the increases observed in the US (12.18%) and photothermal cycling (32.68%) groups (Supplementary Fig. 10d). Additionally, ESR analysis demonstrated that the characteristic signal peaks of $^1O_2$ and $\cdot O_2^-$ under dual laser and US stimulation were stronger than those in individual treatment groups (Supplementary Fig. 23). These findings imply the synergy between PTE and sono-piezoelectric catalysis, significantly enhancing the catalytic performance of BCSO NSs and providing a promising strategy for amplifying ROS generation in catalytic therapy.

To elucidate the underlying PTE and sono-piezoelectric mechanisms, the band structure of BCSO NSs was systematically investigated. Based on VB-XPS analysis, the VB edge of BCSO NSs was determined to be −0.08 eV (Supplementary Fig. 19b). The CB potential was theoretically calculated to be −1.12 V relative to the normal hydrogen electrode (NHE), which is more negative than the redox potential of oxygen/superoxide (−0.33 eV). This energetically favorable alignment suggests that BCSO NSs can efficiently facilitate the conversion of O_2 into $\cdot O_2^-$ under the excitation of external physical fields. A plausible mechanistic pathway involves the induction of an internal electric field upon exposure to US or a temperature gradient, which generates polarization within BCSO NSs. This polarization effect drives spatial separation and directional migration of charge carriers, leading to their accumulation on opposite surfaces, thereby enhancing piezoelectric catalytic reactions[30,46,47]. The electrons enriched in the CB actively reduce oxygen molecules to produce $\cdot O_2^-$, which can be further oxidized to generate $^1O_2$ (Fig. 3n)[48]. Particularly, the band bending and accelerated charge carrier dissociation enabled by PTE and sono-piezoelectric effects can significantly amplify the ROS generation of BCSO NSs[17,49]. This enhanced ROS production contributes to the improved nanocatalytic therapeutic effect, making BCSO NSs highly promising for PTE- or sono-electric-driven therapy.

Apart from their intriguing PTE and sono-piezoelectric effects, BCSO NSs are also expected to generate hydroxyl radicals (·OH) by mimicking POD activity and simultaneously deplete GSH due to the presence of bimetallic elements in their chemical composition (Fig. 3o). The POD-like catalytic activity of BCSO NSs was investigated using 3,3′,5,5′-Tetramethylbenzidine (TMB) as an indicator, where TMB is oxidized by ·OH to form blue-colored oxidized TMB (oxTMB). The characteristic absorbance of oxTMB at around 652 nm significantly increased with higher concentrations of BCSO NSs and H_2O_2 under mildly acidic TME conditions (Supplementary Fig. 24), indicating efficient catalytic ·OH generation. Methylene blue (MB) was utilized as another reagent to further validate the POD-like activity of BCSO NSs. In contrast to TMB, MB reacts with·OH, resulting in the reduction of methylene blue from its oxidized form (blue) to its reduced form (colorless or pale blue). As expected, with increasing concentrations of BCSO NSs and H_2O_2, the absorbance at around 665 nm decreased rapidly (Supplementary Fig. 25). Notably, the POD-like catalytic activity was dramatically diminished under neutral pH conditions (Supplementary Fig. 26), which is advantageous for tumor-specific nanocatalytic therapy. Furthermore, it was hypothesized that the piezoelectric effect of BCSO NSs under US irradiation could enhance their inherent POD-like enzyme activity. This effect was evidenced by a significant increase in the production of oxTMB in the BCSO + US group compared to the single enzyme-mimicking catalytic group without US irradiation (Fig. 3p, Supplementary Fig. 27). Following US irradiation, the characteristic absorption peak of MB in the BCSO US group exhibited a marked reduction compared to the purely catalytic group, demonstrating that US irradiation enhances the enzymatic catalytic efficiency of BCSO NSs (Supplementary Fig. 28). ESR spectra also revealed typical ·OH signal peaks with an intensity ratio of 1:2:2:1 when BCSO NSs reacted with H_2O_2. However, this ·OH signal is diminished after specific scavenging by tertiary butanol, confirming the production of ·OH (Supplementary Fig. 22c). After US treatment, the ·OH signal peak became more pronounced (Fig. 3q). Additionally, the GSH depletion capability of BCSO NSs was examined using the probe 5,5′-dithiobis-(2-nitrobenzoic acid) (DTNB). The reaction of DTNB with GSH produces 5-thio-2-nitrobenzoic acid (TNB), which exhibits a characteristic absorbance at near 412 nm. With increased incubation time between BCSO NSs and GSH, a significant reduction in absorbance was observed (Fig. 3r). Likewise, as the concentration of BCSO NSs increased, the absorbance of TNB at 412 nm correspondingly decreased (Supplementary Fig. 29), suggesting the effectiveness of BCSO NSs in the catalytic depletion of GSH. Given that overexpressed GSH supports intracellular oxidative stress resistance, the combined GSH depletion and ROS generation by BCSO NSs would ensure efficient sono-piezoelectric/enzymatic nanocatalytic therapy.

Computational analysis of multimodal catalytic mechanisms of BCSO NSs

To gain more insight into the catalytic mechanisms, we further performed density functional theory (DFT) calculations to simulate the reaction process. As previously mentioned, BCSO NSs are composed of alternating stacked Bi-O layers and Cu-Se layers, giving rise to the natural heterostructure in this superlattice nanocatalyst. Hence, we hypothesize that their catalytic activity can be enhanced by forming a built-in electric field within the 2D heterostructures. Based on the optimized structural model of layered BCSO NSs, charge density difference (CDD) simulation analysis revealed notable electron transfer from the conductive $[Cu_2Se_2]^{2-}$ sublayer to the $[Bi_2O_2]^{2+}$ sublayer (Fig. 4a), implying the feasibility of forming an internal electric field in BCSO NSs. In the 3D images, yellow electron clouds represent electron gain, while blue electron clouds represent electron loss. After heating to 45 °C or applying a pressure of 1 MPa along the Z-axis, the amount of charge transfer increased from 0.33 e to 0.58 e and 0.65 e, respectively. This indicates that the input of these external energies significantly facilitates more rapid electron transfer within the intrinsic heterostructures of BCSO NSs (Fig. 4b, supplementary Data 1–3). A similar tendency was mirrored by the electronic localization function (ELF) results. After thermal cycling or pressure application, the red electron clouds around Bi and O, as well as the green electron clouds around Cu and Se, became more pronounced (Fig. 4c), implying that these external excitations strengthened the chemical bonding. This increased bonding degree enhanced the charge transfer between the Cu-Se and Bi-O sublayers, thereby amplifying the internal electric field strength between these sublayers and ultimately leading to higher catalytic activity. Additionally, the work function is crucial for understanding the surface electronic properties. Compared to BCSO NSs under ambient conditions, the work function values of BCSO NSs were significantly reduced when activated by heating or mechanical pressure (Fig. 4d). This finding demonstrates that the input of thermal/mechanical energies can improve the electron-transfer process of BCSO NSs, highlighting the advantage of their energy-transformation effects.

Given the semiconductor characteristics of BCSO NSs, their bandgap structure was calculated to evaluate charge mobility under different conditions. Consistently, density of state (DOS) data showed that the bandgap decreased from 1.64 eV to 1.23 eV and 0.72 eV after the incorporation of heating or mechanical pressure, respectively (Fig. 4e). This reduction indicates that the thermal/mechanical energies can effectively shorten the carrier migration distance, thereby facilitating charge mobility and enhancing the catalytic activity. Moreover, the band structure properties of BCSO NSs can be tailored through either the PTE or the piezoelectric effect[50]. The polarization of BCSO NSs under thermal or mechanical energy stimulations results in

https://doi.org/10.1038/s41467-025-61041-4

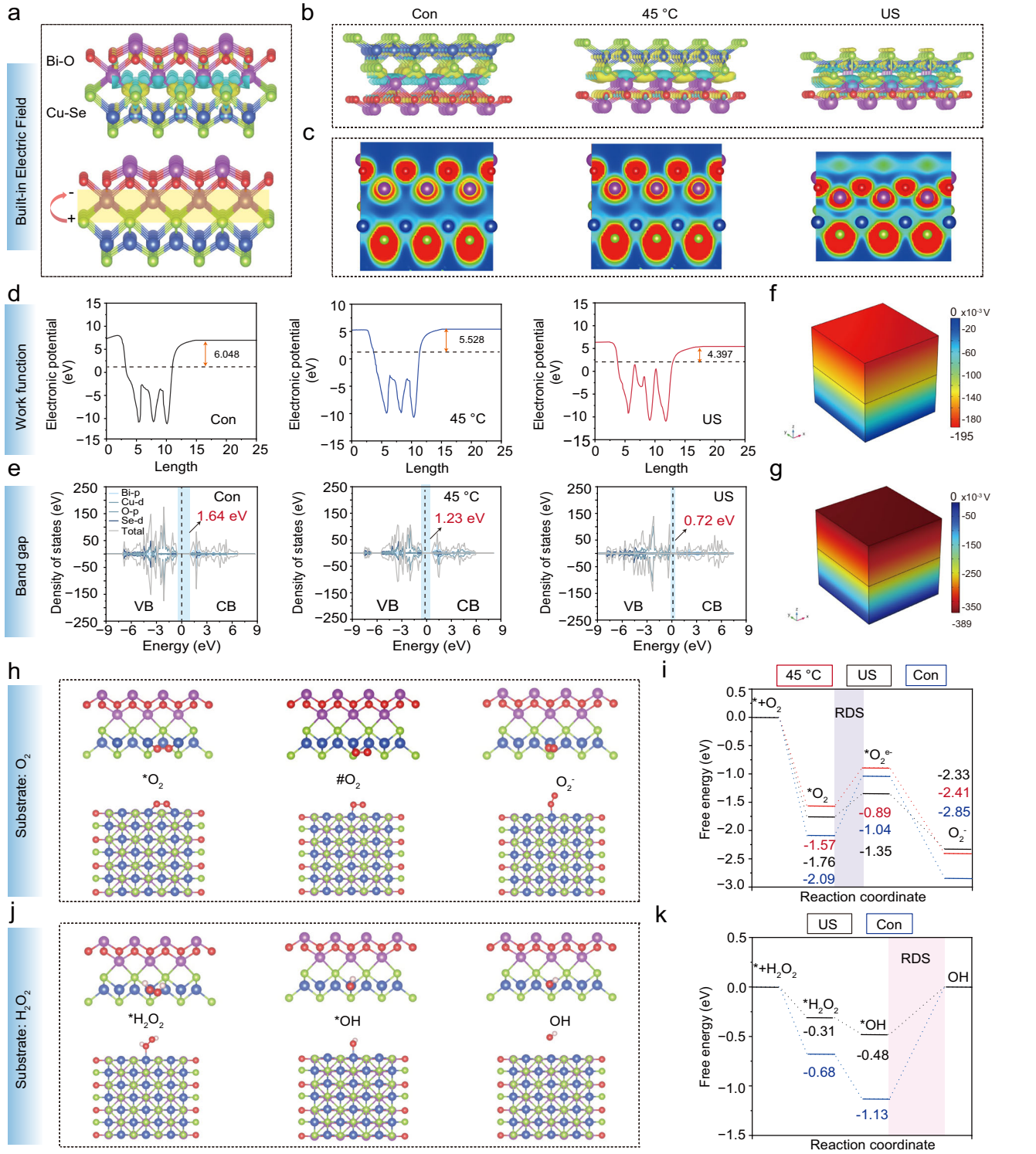

Fig. 4 | Computational calculations of the catalytic mechanism of BSCO NSs. **a** Schematic illustration of differential charge data to explain the catalytic mechanism. **b** Differential charge distributions of BCSO NSs under no external conditions, thermal cycling, and pressurized conditions, respectively. **c** Local electronic density of BCSO NSs under the above conditions. **d** Planar-averaged electrostatic potential for each condition. **e** DOS profiles under no external conditions, thermal cycling, and pressurized conditions. **f** COMSOL simulation for PTE potential distribution in BCSO NSs under 15 °C of temperature difference. **g** COMSOL simulation for sono-piezoelectric potential distribution in BCSO NSs under a pressure of 1 MPa. Simulated surface configurations of initial, transition, and final states for (**h**) oxygen adsorption and (**i**) POD-like enzyme catalytic processes. The reaction energy diagrams simulate (**j**) oxygen adsorption and (**k**) POD-like enzyme catalytic processes. Source data are provided as a Source Data file.

an internal fields within their structures, thereby altering its functional performance and catalytic activity. To distinctly visualize these microscale alterations, finite element simulations were conducted using the COMSOL multiphysics software package. These simulations can provide direct insights into the potential distribution in BCSO NSs under various external stimuli, specifically under a mechanical pressure of 1 MPa and a thermal gradient of 15 °C (Fig. 4f, g, Supplementary Fig. 30). The simulation results revealed a gradual distribution of potential along the z-axis in the BCSO NSs upon the input of external physical energies. The thermoelectric potential difference of 0.18 V and the piezoelectric potential difference of 0.35 V not only provide sufficient energy for charge carrier transport but also facilitate further modulation of the band structure, thereby enhancing charge mobility and catalytic reactions.

Furthermore, the impact of external energy activation on the catalytic performance of BCSO NSs was studied by DFT calculation. The proposed reaction mechanisms for the generation of $\cdot O_2^-$ and ·OH were correspondingly presented. For PTE or piezoelectric-catalyzed generation of $\cdot O_2^-$, the Cu sites at the atomic interface are more likely to adsorb and dissociate molecular O_2 (Fig. 4h). The formation of $^*O_2^{e^-}$ is identified as the rate-determining step (RDS) in the catalytic reaction of BCSO NSs for generating $\cdot O_2^-$. After the application of heating or 1 MPa pressure, the energy required for the RDS decreased from 1.05 eV to 0.68 eV and 0.41 eV, respectively, indicating that BCSO NSs exhibit improved catalytic activity under PTE and sono-piezoelectric activations (Fig. 4i). Similarly, the key intermediate pathway of the POD-like enzyme reaction was illustrated, where H_2O_2 molecules are adsorbed onto Cu sites, and the adsorbed $H_2O_2^*$ uniformly dissociates into two OH* (Fig. 4j). It can be seen that the process of OH* forming ·OH is endothermic, representing the RDS in the POD catalytic process. The free energy barrier throughout the reaction process decreased from 1.13 eV under ambient conditions to 0.48 eV under mechanical pressure (Fig. 4k), which may explain the enhanced catalytic activity of BCSO NSs under US irradiation. Additionally, when a temperature gradient and mechanical pressure are applied along the z-axis, the layered heterostructure of BCSO NSs undergoes compression, reducing the lattice parameter in the z-direction and shortening the Bi-Se distance (Supplementary Figs. 31–33). This compression facilitates intra-layer charge transfer, thereby enhancing the catalytic activity. Taken together, it is deduced that the inherently layered heterostructures significantly contribute to the narrow bandgap and external field-responsive properties of BCSO NSs. The internal electric field, activated by thermal-cooling cycles and mechanical pressure, facilitates efficient electron-hole pair separation and suppresses their recombination, thereby extending carrier lifetimes and enhancing catalytic ROS generation.

In vitro PTE catalytic antibacterial activity of superlattice BCSO NSs

Taking advantage of their NIR light-triggered energy transformation capability, BCSO NSs were utilized for antibacterial applications using a wound infection model. First, their in vitro antimicrobial activity was investigated against typical Gram-negative *Escherichia coli* (*E. coli*) and Gram-positive methicillin-resistant *Staphylococcus aureus* (MRSA) pathogens. The on/off cycle of 1064 nm laser illumination enables controlled temperature fluctuations, thereby facilitating ROS production through PTE effects, ensuring effective bacterial eradication (Fig. 5a and Supplementary Fig. 34)[51]. The intracellular levels of ROS in bacteria were detected using the 2,7-dichlorodihydrofluorescein diacetate (DCFH-DA, green fluorescence) staining method[52]. Intense green fluorescence can be found in the samples treated with BCSO NSs and NIR-triggered heating/cooling cycles, indicating that PTE effects of BCSO NSs induced substantial intracellular ROS (Fig. 5b). The living-dead staining method was utilized to further evaluate the antibacterial efficacy[53]. Consistent with the tendency of ROS generation, the PTE catalytic group exhibited the most pronounced red fluorescence, suggesting its high efficiency in killing bacteria (Fig. 5c). Quantitative analysis showed that *E. coli* and MRSA treated with BCSO NSs and laser cycling exhibited significantly higher red fluorescence intensities of 57.05% and 96.55%, respectively (Fig. 5d, e), suggesting that MRSA was more sensitive to the PTE catalytic therapy than *E. coli*. Furthermore, plate colony-counting results revealed that both types of bacteria were completely eradicated after the treatment of BCSO NSs upon on/off NIR illumination cycles (Fig. 5g, h). We also employed scanning electron microscopy (SEM) to assess morphological alterations of bacteria under varied treatments. While bacteria in untreated and mere NIR irradiation groups exhibited intact morphology with smooth and intact cell envelopes, the PTE catalytic treatment resulted in significant membrane distortion, wrinkling, and shrinkage on the bacterial surface (Fig. 5i). TEM images showed that significant cytoplasmic disorganization and large-area vacuolization can be observed in bacteria exposed to BCSO NSs plus laser on/off cycle (Fig. 5j). These findings demonstrate that the PTE catalytic therapy enabled by 2D superlattice nanocatalysts can effectively induce bacterial lethality.

To elucidate the antibacterial mechanism of BCSO NSs against MRSA, RNA sequencing identified 331 differentially expressed genes (DEGs) in the PTE catalytic group compared to the untreated control. Hierarchical clustering revealed specific upregulated and downregulated genes (Supplementary Fig. 35). Gene Ontology (GO) analysis showed that BCSO NSs combined with NIR laser on/off cycling disrupted key biological processes, including antioxidant mechanisms, ATP-dependent functions, and transcriptional regulation (Fig. 5l). The Kyoto Encyclopedia of Genes and Genomes (KEGG) pathway analysis revealed significant alterations in bacterial cellular processes, metabolism, and genetic information processing, with enrichment in pathways related to amino acid, carbohydrate, energy, and lipid metabolism (Fig. 5m). Enrichment in gene replication and repair pathways indicated that PTE treatment impaired bacterial regeneration. Overall, these transcriptomic results suggest that BCSO NSs combined with laser treatment exert antibacterial effects by disrupting bacterial intracellular homeostasis.

In vivo PTE catalytic eradication of MRSA-induced wound infection

Next, in vivo PTE antibacterial efficacy of BCSO NSs was evaluated by an MRSA infection model (Fig. 6a). Thermal cycling at the wound site was conducted using 1064 nm NIR-II light for precise heating and cooling (Supplementary Fig. 36). After the treatments, all groups showed scab formation and wound contraction. Notably, the BCSO + laser group achieved almost closed wounds with scab detachment by day 9, highlighting the high efficacy of the PTE catalytic treatment in bacteria eradication and wound healing (Fig. 6b–d). Furthermore, there were no significant changes in the body weight of all mice during the treatment period, indicating that the treatments caused negligible adverse effects (Fig. 6e). Furthermore, hematoxylin & eosin (H&E) stained images showed that the untreated and laser-treated samples exhibited marked inflammatory cell infiltration and extensive non-structural necrosis in the epithelial defect areas. On the contrary, those inflammatory symptoms were effectively alleviated in dermal tissue treated with BCSO + laser (Fig. 6f). Moreover, in contrast to the disorganized structure of collagen fibers in other groups, the PTE catalytic treatment resulted in newly formed collagen fibers under the intact epithelium, as evidenced by Masson's trichrome staining images (Fig. 6g). Additionally, CD31 immunohistochemical staining was used to assess angiogenesis in the dermal tissue. As expected, the fluorescent images revealed the regeneration of blood vessels in the newly formed tissue after the stimulation of BCSO NSs upon on/off laser cycling (Fig. 6h). To evaluate the potential adverse effects of

https://doi.org/10.1038/s41467-025-61041-4

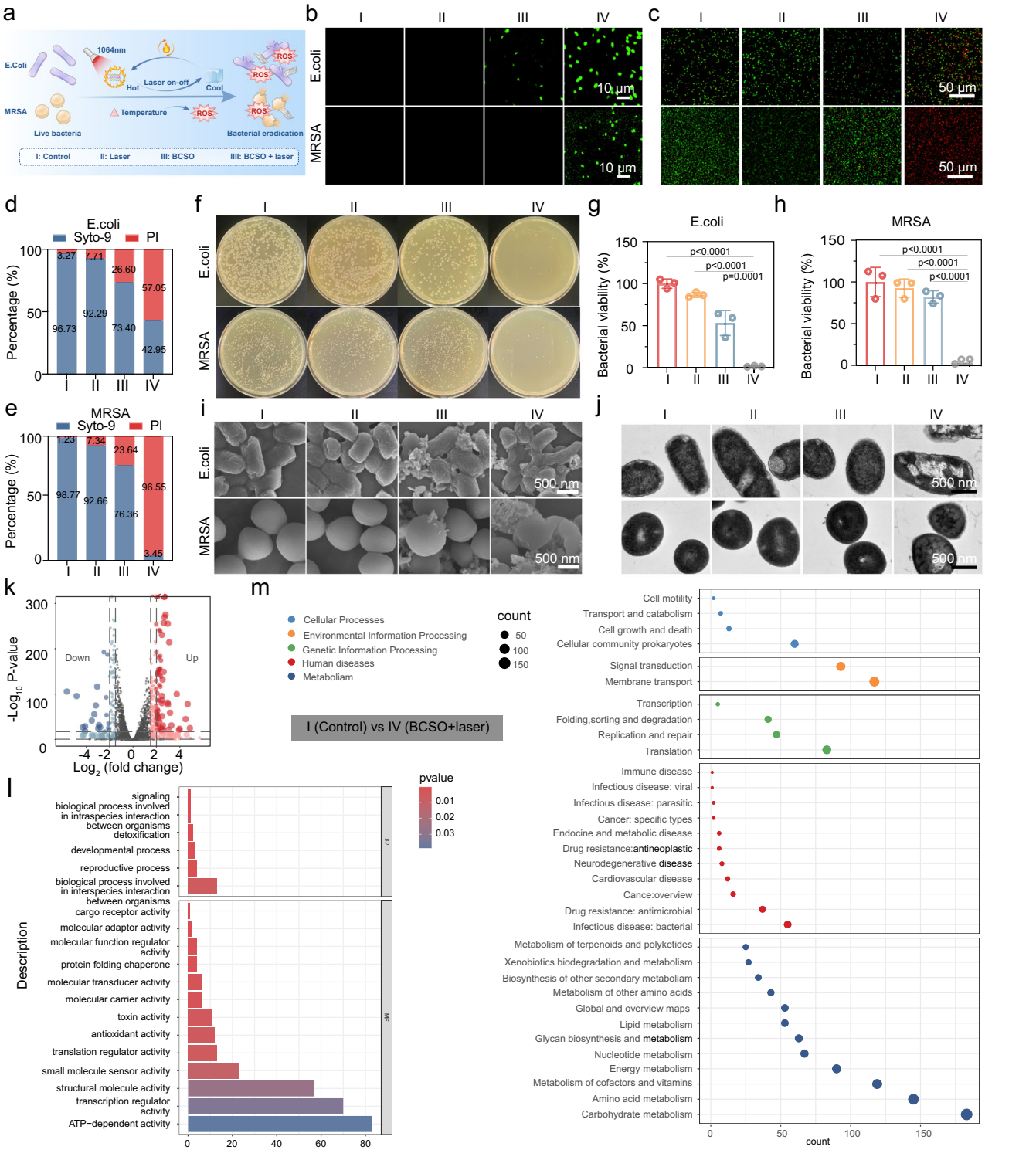

Fig. 5 | In vitro antibacterial activity of BCSO NSs. a Schematic illustration of the bacteria-killing ability of BCSO NSs upon NIR-II laser irradiation. **b** Fluorescence images of intracellular ROS in *E.coli* and MRSA. **c** CLSM images of *E.coli* and MRSA after various treatments stained with SYTO9 and PI. Analysis of the fluorescence intensity ratio corresponding to live/dead bacteria of (**d**) *E.coli* and (**e**) MRSA following various treatments. **f** *E.coli* and MRSA's viability under different treatments tested by agar plate method. Corresponding quantitative analysis of (**g**) *E. coli* and (**h**) MRSA colony after different treatments ($n = 3$ independent biological samples, mean ± s.d., one-way ANOVA with Dunnett's test). **i** SEM and (**j**) bio-TEM images of *E. coli* and MRSA after different treatments. **k** Volcano plot for the distribution of DEGs ($n = 3$ independent biological samples, $\log_2$ fold change ≥2, two-tailed). **l** GO enrichment analysis of DEGs ($n = 3$ independent biological samples, $\log_2$ fold change ≥ 2, two-tailed). **m** KEGG enrichment pathway analysis in different groups ($n = 3$ independent biological samples, $\log_2$ fold change ≥2, two-tailed). Source data are provided as a Source Data file.

https://doi.org/10.1038/s41467-025-61041-4

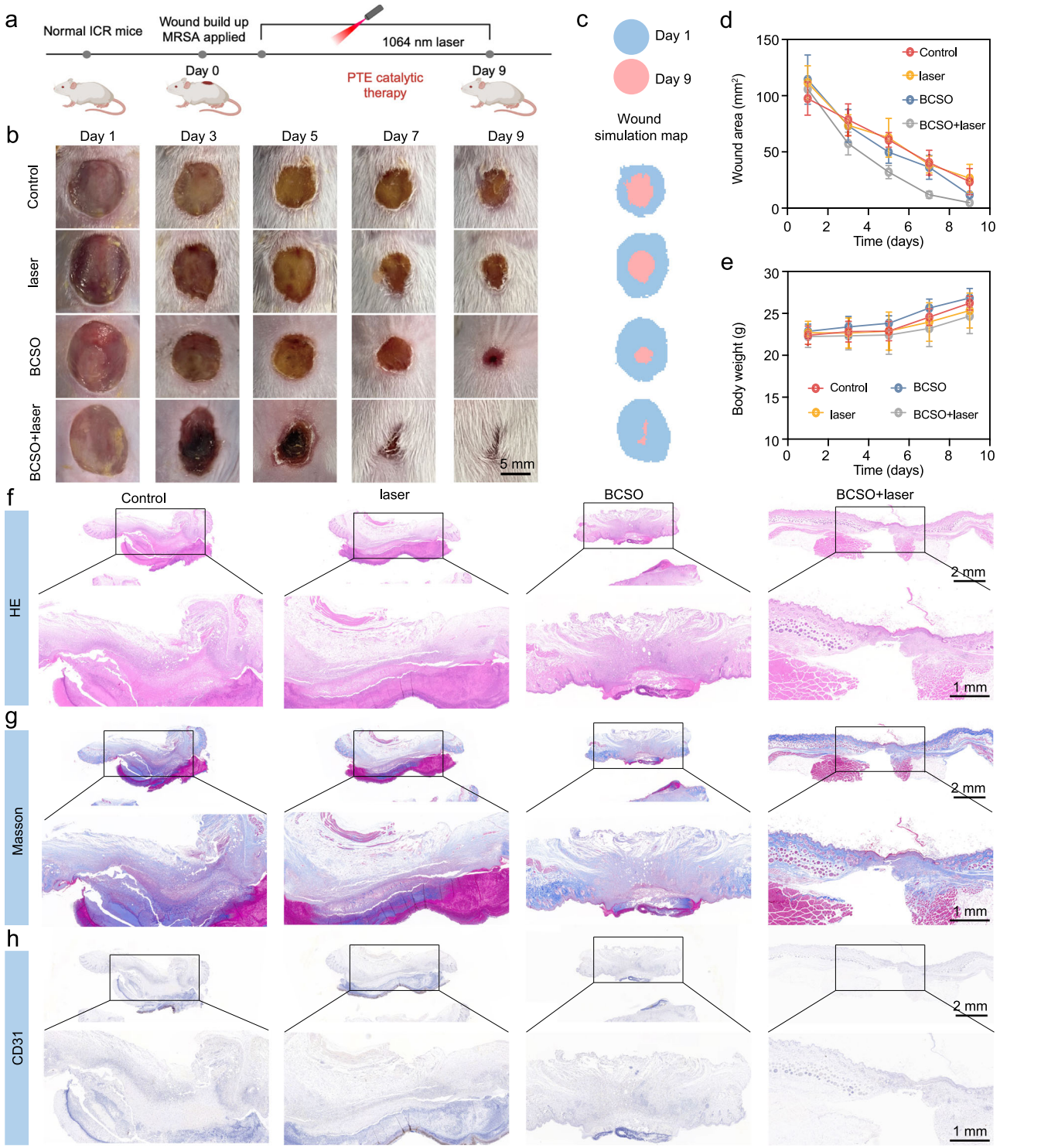

Fig. 6 | In vivo eradication of MRSA-induced wound infection. a Schematic illustration of the wound infection model establishment and PTE therapy by BCSO NSs (Created with BioRender.com). **b** Representative photographs of the wound healing process. **c** Wound simulation maps on day 1 and 9 in each group. **d** Wound area and (**e**) body weight for each group of mice recorded after various treatments ($n = 5$ mice per group, mean ± SD.). **f** H&E staining images, (**g**) Masson staining images, and (**h**) CD 31 immunohistochemical staining images of dermal tissues around wound sites from different groups harvested on day 9. Source data are provided as a Source Data file.

prolonged exposure to BCSO NSs in mice, major organs were harvested at intervals of 1, 7, and 14 days post-application of BCSO NSs to murine wounds. Copper (Cu) and bismuth (Bi) concentrations within these tissues were quantitatively analyzed using inductively coupled plasma optical emission spectroscopy (ICP-OES) (Supplementary Fig. 37). The results indicated that the levels of Cu and Bi in treated mice exhibited no significant deviations compared to the control group. Furthermore, histopathological assessments of the heart, liver, spleen, lungs, and kidneys were performed using H&E staining (Supplementary Fig. 38). These examinations revealed negligible organ damage or inflammatory responses in the mice treated with BCSO NSs, indicating their excellent biocompatibility without eliciting acute or

chronic toxicity. These in vivo results corroborate that the PTE effects of BCSO NSs can eliminate wound infections by catalyzing ROS generation through energy transformation.

In vitro sono-piezoelectric sensitized nanocatalytic anticancer efficacy

The above-demonstrated sono-piezoelectric effect, synergizing with the inherent catalytic activity of BCSO NSs, is expected to facilitate the interconversion of energy types, leading to efficient ROS generation and improved therapeutic efficacy against cancer cells. Thus, a series of cellular experiments were conducted to validate the sono-piezoelectric enhanced anticancer efficacy. Intriguingly, human umbilical vein endothelial cells (HUVECs) incubated with the BCSO NSs displayed ignorable cell death even at a high concentration of 400 μg/mL, indicating the favorable biocompatibility of superlattice NSs (Fig. 7a). Conversely, a positive correlation between the increased concentration of BCSO NSs and cell mortality was observed when melanoma cells (B16F10) were treated for the same durations (Fig. 7b). A similar trend was evident in 4T1 breast cancer cells and H22 liver cancer cells (Supplementary Fig. 39). Such tumor-specific cytotoxicity is likely attributed to the disruption of intracellular homeostasis caused by the enzyme-like catalytic activity of BSCO NSs, which mediates the transformation of endogenously abundant H_2O_2 and GSH in cancer cells.

Next, flow cytometry (FCM) was employed to monitor the cellular uptake of FITC-labeled BCSO NSs by B16F10 cells over various time intervals. The results demonstrated a time-dependent increase in FITC fluorescence intensity (Fig. 7c). Confocal laser scanning microscopy (CLSM) images showed the enhanced accumulation of green fluorescence spots in B16F10 cells, visualizing the efficient internalization of BCSO NSs (Fig. 7d). Additionally, subcellular distribution of FITC-labeled BCSO NSs was investigated using lysotracker and mitotracker. It can be seen that only a small portion of green fluorescence was co-localized with red spots that represent lysosomes (Supplementary Fig. 40), suggesting the lysosomal escape ability of BCSO NSs. Besides, the overlapping of BCSO NSs and mitochondria was not observed (Supplementary Fig. 41). To evaluate the sono-piezoelectric ROS production in B16F10 cells by BCSO NSs, the DHE probe was utilized to measure intracellular $\cdot O_2^-$ levels. A marked increase in the red fluorescence intensity of DHE confirmed the substantial generation of $\cdot O_2^-$ in the BCSO NSs group only upon US activation (Fig. 7e, Supplementary Fig. 42). Additionally, intracellular fluorescence imaging with the ROS probe (DCFH-DA, green) revealed that cells in the BCSO NSs group exhibited moderate green fluorescence. This can be ascribed to the generation of ·OH due to the POD-like catalytic activity and GSH depletion capability of BCSO NSs. In contrast, the BCSO + US group showed much more intense green fluorescence, implying that sono-piezoelectric catalysis effectively promotes extensive ROS generation in B16F10 cells (Fig. 7f, Supplementary Fig. 43). The therapeutic efficacy of sono-piezoelectric treatment on B16F10 cells was further evaluated using the calcein-AM/PI co-staining assay. Compared to the large areas of green fluorescence observed in the control and US groups, cells treated with BCSO NSs exhibited a portion of red-labeled dead cells. Notably, sono-piezoelectric catalytic treatment led to significant cell death of B16F10 cells, as evidenced by the intense red fluorescence (Fig. 7g). The cytotoxic efficacy of various treatments on cancer cells was quantitatively evaluated using the cell counting kit-8 (CCK-8) assay. Cells were incubated with BCSO NSs at a concentration of 200 μg/mL for 12 h and then exposed to low-intensity US irradiation (1 W cm^{-2}, 1 MHz, 50% duty cycle). CCK-8 data indicated that the survival rate of B16F10 cells treated with only BCSO NSs was reduced to 68.3% (Fig. 7h). The BCSO NSs + US group exhibited the most significant cytotoxic effect with a high cell mortality of 89.8%. These outcomes demonstrate that the combined sono-piezoelectric effects and catalytic activity of BCSO NSs can effectively kill cancer cells, achieving satisfactory antitumor efficacy.

Subsequently, FCM was utilized to quantitatively assess apoptosis in B16F10 cells (Fig. 7i). The total apoptosis rates (early plus late apoptosis) induced by mere BCSO NSs and sono-piezoelectric catalytic treatment were 20.8% and 34.9%, respectively. This trend underscores the superior efficacy of sono-piezoelectric catalytic therapy in inducing apoptosis in B16F10 cells (Fig. 7j). To further elucidate the mechanism of cellular apoptosis, mitochondrial membrane potential changes in B16F10 cells were evaluated using the JC-1 staining assay[54]. Red fluorescence, representing J-aggregates, indicates stable mitochondrial membrane potentials, while green fluorescence representing J-monomers suggests diminished potentials. CLSM images from the control group exhibited distinct red fluorescence. BCSO NSs alone induced only a moderate reduction in the mitochondrial membrane potential of B16F10 cells. However, a significant increase in green JC-1 monomers was observed in cells treated with BCSO NSs upon US irradiation, indicative of mitochondrial dysfunction induced by sono-piezoelectric ROS accumulation (Fig. 7k). Additionally, similar results were detected through FCM analysis (Supplementary Fig. 44). These findings substantiate that the engineered BCSO NSs can mediate combined energy transformation catalytic therapy to induce severe oxidative damage, thereby triggering cell apoptosis for efficient antitumor treatment (Fig. 7l).

Mechanistic investigation of ferroptosis triggered by combined energy transformation nanocatalytic therapy

GSH is a critical contributor in resisting intracellular oxidative stress, which significantly counteracts the effectiveness of ROS-mediated cell killing. We hypothesize that the GSH depletion capability of BCSO NSs can enhance antitumor efficacy. To elucidate the synergistic effect of GSH depletion and ROS accumulation in inducing cell death, we employed the thiol-tracker violet fluorescence probe to measure the intracellular GSH levels in B16F10 cells after various treatments[55]. CLSM images and corresponding semi-quantitative data indicated a decreased fluorescence signal in cells co-incubated with BCSO NSs compared to the control, signifying the remarkable GSH-depleting capability of BCSO NSs. Furthermore, the blue fluorescence intensity in the BCSO + US group was significantly lower than that in other groups, suggesting that the catalytically generated ROS further consumes intracellular GSH (Fig. 8a, b). The GSH-depleting ability of BCSO NSs was further investigated using a GSH assay kit. Quantitative results showed the intracellular GSH concentrations of 37.9 μmol L^{-1} in the control group and 40.6 μmol L^{-1} in the US group, which dropped to 27.4 μmol L^{-1} with BCSO NSs treatment. Upon US exposure, GSH concentration further decreased to 11.8 μmol L^{-1} (Fig. 8c). These findings are consistent with the aforementioned CLSM analysis results.

Extensive accumulation of ROS and depletion of GSH in B16F10 cells intensified oxidative stress, impacting the expression of apoptotic proteins, including the pro-apoptotic protein BAX and the anti-apoptotic protein Bcl-2[56–58]. Western blot analysis revealed significantly upregulated expression of BAX protein in the BCSO + US group, suggesting enhanced BAX oligomerization under sono-piezocatalytic effects (Fig. 8d, e, Supplementary Fig. 45)[59,60]. Meanwhile, cells treated with BCSO NSs alone showed reduced Bcl-2 expression, indicating that the inherent anti-apoptotic mechanism of tumor cells was partially reversed by the superlattice nanocatalysts[61]. This pro-apoptotic activity of BCSO NSs was further enhanced in the presence of US irradiation (Fig. 8d, f, Supplementary Fig. 45). Moreover, GPX4, an enzyme that inhibits ferroptosis, was downregulated in response to GSH depletion[62,63]. The GPX4 band was notably weaker in the BCSO + US group compared to other groups, suggesting that the combined sono-piezoelectric and enzymatic nanocatalytic therapy mediated by BCSO NSs effectively induced GPX4 protein

https://doi.org/10.1038/s41467-025-61041-4

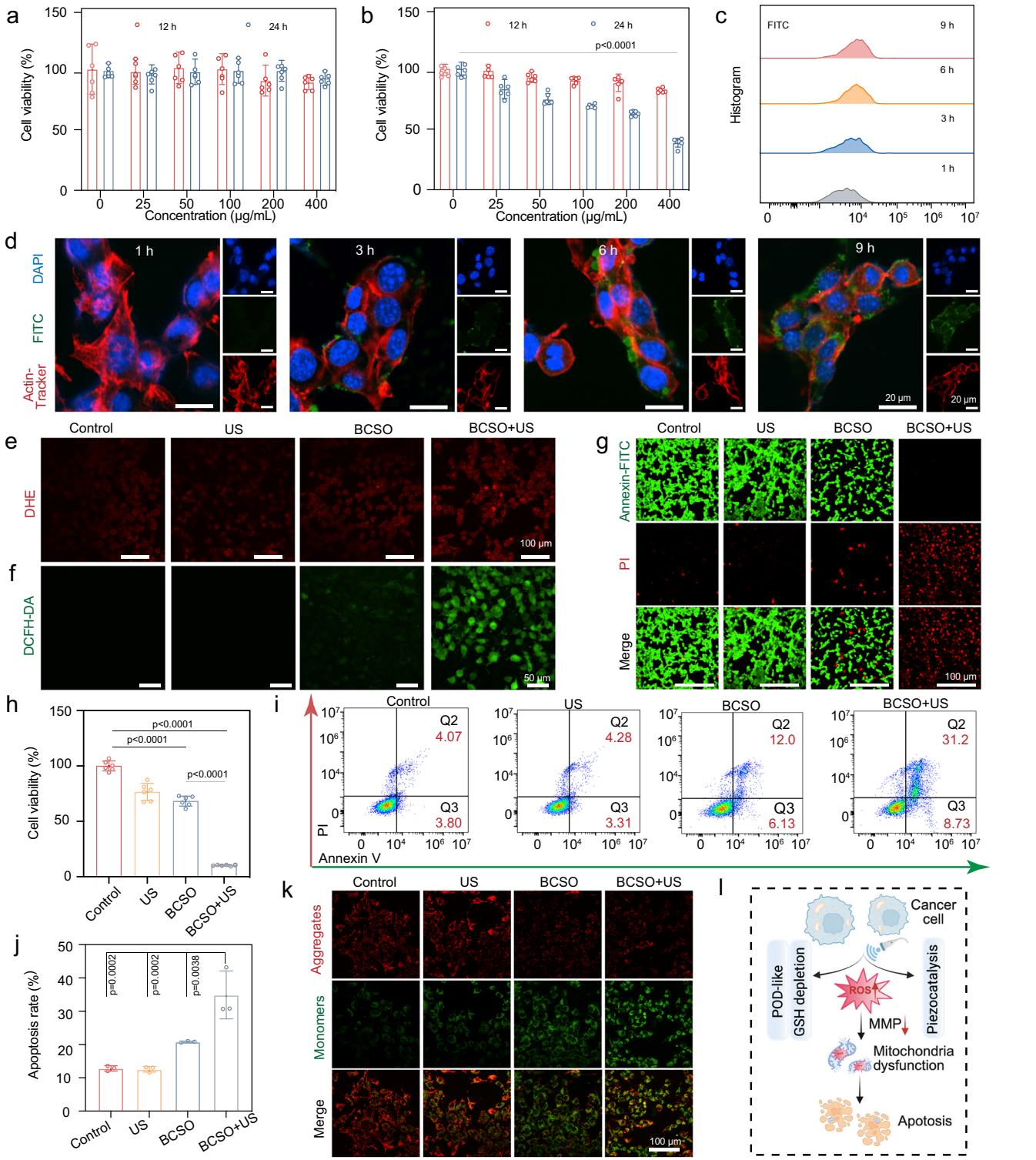

Fig. 7 | In vitro ROS generation and nanocatalytic therapeutic performance of BCSO NSs against B16F10 cells. Viability of (**a**) HUVEC and (**b**) B16F10 cells after incubation with various concentrations of BCSO NSs for different time ($n = 6$ independent biological samples, mean ± s.d., two-way ANOVA). **c** FCM images and **d** CLSM images of B16F10 cells after incubation with FITC-labeled BCSO NSs. **e** CLSM images of DCFH-DA-stained B16F10 cells under various treatments. **f** Intracellular $\cdot O_2^-$ level of B16F10 cells after different treatments. **g** Live/dead staining of B16F10 cells in different groups. **h** Cytotoxicity assays of B16F10 cells across groups ($n = 6$ independent biological samples, mean ± s.d., one-way ANOVA). **i** FCM images of the apoptosis of B16F10 cells and (**j**) the corresponding quantitative analysis of apoptosis percentages in different groups ($n = 3$ independent biological samples, mean ± s.d., one-way ANOVA with Dunnett's test). **k** CLSM images of JC-1-stained B16F10 cells following different treatments. **l** Schematic of the sono-piezoelectric nanocatalytic therapy (Created with BioRender.com). Source data are provided as a Source Data file.

https://doi.org/10.1038/s41467-025-61041-4

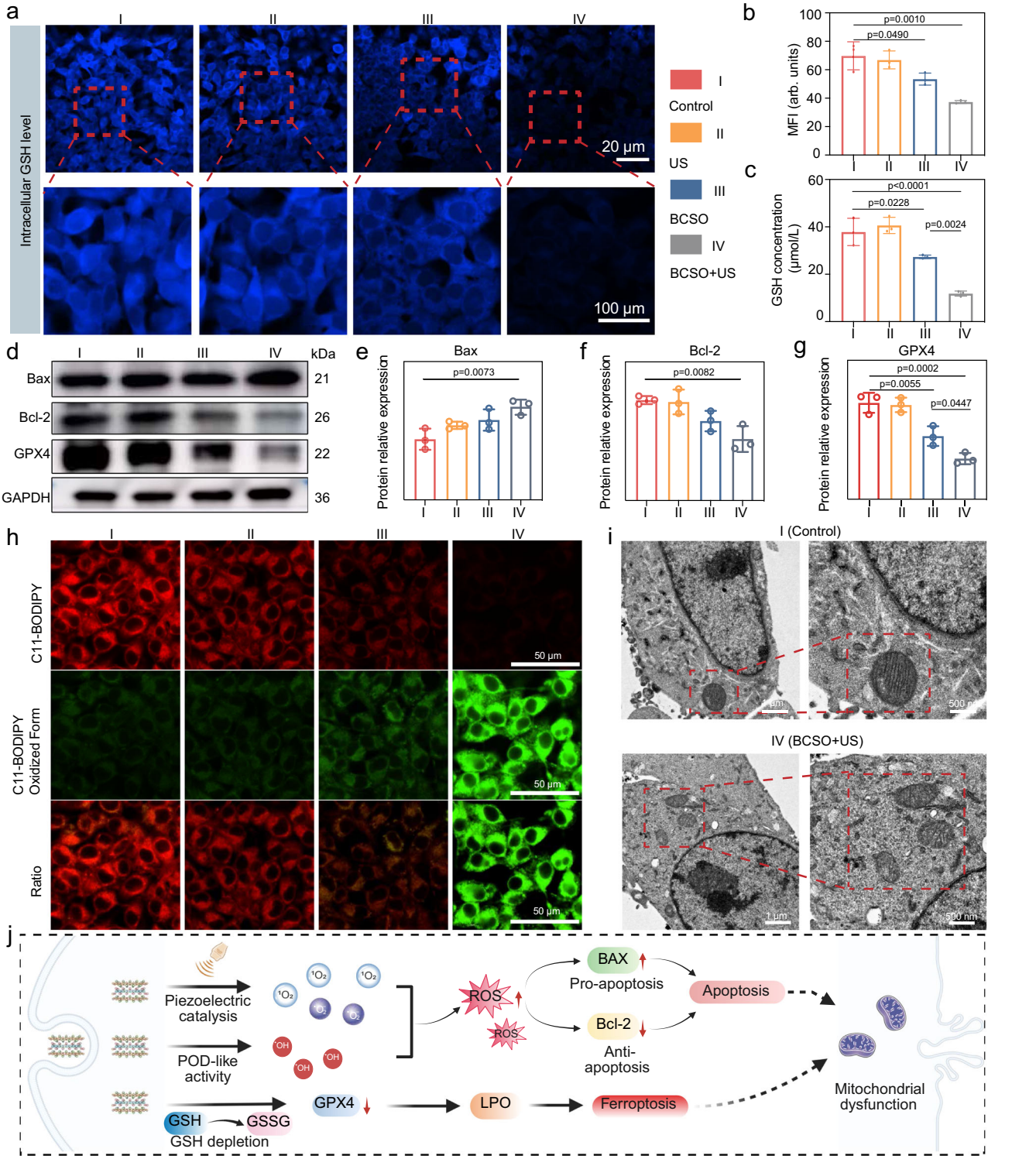

Fig. 8 | Sono-piezoelectric sensitized nanocatalytic ferroptosis and apoptosis by BCSO NSs. a CLSM observation and (**b**) corresponding quantitative fluorescent intensity of intracellular GSH level ($n = 3$ independent biological samples, mean ± s.d., one-way ANOVA with Tukey's post hoc test,). **c** Quantification of GSH concentration in B16F10 cells ($n = 3$ independent biological samples, mean ± s.d., one-way ANOVA with Tukey's post hoc test). **d** Western blot analysis and the corresponding semi-quantitative analysis of (**e**) GPX4, (**f**) Bax, and (**g**) Bcl-2 ($n = 3$ independent biological samples, mean ± s.d., one-way ANOVA. Samples in different blots were derived from the same experiment and processed in parallel under identical conditions). **h** CLSM images of the intracellular distribution of LPO. **i** Bio-TEM images of B16F10 cells in different groups. The red box indicates the mitochondria. **j** Schematic of the proposed mechanism of sono-piezoelectric nanocatalysis (Created with BioRender.com). Source data are provided as a Source Data file.

downregulation in B16F10 cells (Fig. 8d, g, Supplementary Fig. 45). These results support the hypothesis that BCSO-mediated GSH depletion and enhanced ROS production can deactivate GPX4 to promote ferroptosis, thereby amplifying the pro-oxidative catalytic therapeutic efficacy.

Lipid peroxidation (LPO) is a key biological marker of ferroptosis[64]. GPX4 regulates cellular antioxidant capabilities, combats LPO accumulation, and maintains lipid bilayer membrane stability[65]. Thus, the downregulation of GPX4 mediated by BCSO NSs could lead to LPO accumulation and ferroptosis. To assess LPO occurrence in B16F10 cells, we utilized the LPO-specific fluorescent probe C11-BODIPY$^{581/591}$ [66]. When C11-BODIPY$^{581/591}$ is oxidized by LPO, its fluorescence emission shifts from 590 nm (red) to 510 nm (green). Predictably, cells treated with BCSO NSs + US displayed the brightest green fluorescence and the dimmest red fluorescence, indicating the highest LPO levels (Fig. 8h). Bio-TEM revealed ferroptosis-associated morphological changes due to extensive LPO accumulation. Notable reductions in mitochondrial size, increased mitochondrial membrane density, and disruption of mitochondrial cristae were observed post BCSO + US treatment (Fig. 8i). Therefore, the sono-piezoelectric effects and catalytic activity of BCSO NSs enable simultaneous intracellular ROS accumulation and GSH depletion, resulting in GPX4 downregulation and enhanced LPO. This cascade efficiently induces ferroptosis, synergizing with apoptosis to amplify therapeutic efficacy (Fig. 8j).

In vivo sono-piezoelectric nanocatalytic therapeutic efficacy of BCSO NSs against melanoma

Encouraged by the promising in vitro therapeutic efficacy of BCSO NSs, we further conducted in vivo evaluations to assess biocompatibility and melanoma eradication efficacy. First, healthy male ICR mice were intravenously injected with BCSO NSs at doses of 10 mg kg^{-1} or 20 mg kg^{-1} and monitored for 7, 14, and 21 days before euthanasia. Control mice received saline injections. Biochemical analyses of blood revealed negligible impact of BCSO NSs on liver and kidney function markers, such as alanine transaminase, aspartate transaminase, alkaline phosphatase, blood urea nitrogen, and creatinine (Supplementary Fig. 46). Routine blood tests remained within normal reference ranges, indicating commendable hematocompatibility of BCSO NSs (Supplementary Fig. 47). Additionally, major organs (heart, liver, spleen, lung, and kidney) of the mice were collected for H&E staining. Histopathological analysis showed no significant damage or inflammation post-intravenous injection, further substantiating the satisfactory histocompatibility of BCSO NSs (Supplementary Fig. 48). The absence of acute or chronic toxicity and side effects underscores the high biosafety of BCSO NSs, permitting further in vivo applications.

Subsequently, we employed the B16F10 xenograft melanoma model to further evaluate the in vivo antitumor efficacy (Fig. 9a). Due to the notable photonic-to-thermal energy transformation capability exhibited by BCSO NSs in vitro, their potential as a contrast agent for PA imaging was first assessed. The acoustic pressure signals of BCSO aqueous solutions at various concentrations were recorded, demonstrating a linear correlation between PA signal intensity and BCSO NSs dosage (Fig. 9b, Supplementary Fig. 49). Furthermore, following intravenous administration of BCSO NSs via the tail vein, PA signals in the tumor region were monitored at various time points (Fig. 9c). The PA signal in the tumor region reached its peak 6 h post-injection, followed by a gradual decline in intensity, indicating maximum accumulation of BCSO NSs at the tumor site. The favorable PA imaging performance of BCSO NSs highlights their potential for PA imaging-guided therapeutic applications.

To assess tumor inhibition efficacy of BCSO NSs, BALB/c nude mice bearing B16F10 tumors were randomly divided into four groups when the tumor volume reached ~50 mm^3. saline (control), US (1 MHz, 50% duty cycle, 1 W cm^{-2}), only BCSO NSs, and BCSO NSs + US (20 mg kg^{-1}) groups. For the US and BCSO + US groups, US irradiation was applied to the tumor site for 10 min at 6 h post-injection. Over a 12 day observation period, the BCSO group exhibited moderate tumor inhibition compared to mice treated with saline and the US alone, while the BCSO NSs + US group showed significantly inhibited tumor growth (Fig. 9d, h). Tumor weights and photographs of excised tumors corroborated these findings (Fig. 9e, f). Notably, the BCSO + US group exhibited an increased inhibition rate of 91.7%, compared to 57.7% in the BCSO group, suggesting superior antitumor efficacy of sono-piezoelectric nanocatalytic therapy (Fig. 9g). This can be explained by the induction of ferroptosis in tumor cells by BCSO NSs and the piezoelectric-amplified catalytic oxidative damage. Furthermore, negligible significant weight loss was observed in all experimental mice during the treatment period (Fig. 9i). H&E staining images of major organs from each group revealed no apparent tissue damage at the end of the treatment cycle (Supplementary Fig. 50), highlighting minimal side effects or biotoxicity of nanocatalytic therapy.

To elucidate the tumor inhibition mechanism by superlattice BCSO NSs, the GPX4 and ROS levels in tumor tissues from different treatment groups were measured through immunofluorescent staining. As expected, the BCSO NSs group showed decreased GPX4 immunofluorescence in tumor tissues, with a heightened downregulation under US irradiation (Fig. 9j). This suggests that the enhanced antitumor effect of BCSO NSs may be attributed to ferroptosis amplified by the sono-piezoelectric effect. Additionally, ROS levels in tumor tissues were significantly higher in the BCSO + US group than in other groups, indicating that the combined effects of sono-piezoelectric effects and enzyme-like catalytic activity can synergistically guarantee in vivo ROS accumulation (Fig. 9k). Moreover, terminal deoxynucleotidyl transferase dUTP nick end labeling (TUNEL) staining revealed a marked increase in apoptotic cells in the group treated with sono-piezoelectric nanocatalysis (Fig. 9i). Tumor sections from this group exhibited more pronounced necrosis and nuclear deformation and a significantly reduced proportion of Ki-67 positive tumor cells (Fig. 9m, n). Collectively, these in vivo results demonstrate that BCSO NSs upon US irradiation achieve significant antitumor efficacy without causing adverse effects, thus highlighting the potential of sono-piezoelectric nanocatalytic therapy for other therapeutic applications.

In vivo synergistic nanocatalytic therapeutic efficacy of BCSO NSs against deep-seated hepatocellular carcinoma

The PTE and sono-piezoelectric effects of BCSOs have demonstrated promising therapeutic efficacy in wound infection and melanoma. To further highlight the advantages of BCSO-enabled multimodal energy transformation catalysis, we employed an orthotopic luciferase-expressing H22 hepatocarcinoma model to evaluate the synergistic antitumor potential of combined sono-piezoelectric and PTE therapies[67,68]. H22 tumor cells transfected with the luciferase gene were surgically implanted into the livers of nude mice. In vivo bioluminescence results demonstrated significant tumor growth inhibition on day 13 in the group of combined sono-piezoelectric and PTE nanocatalytic therapy (Supplementary Fig. 51a). Semi-quantitative analysis of the bioluminescence further indicated that no marked difference was observed in tumor suppression between the PTE group and the BCSO group, possibly due to the limited penetration depth of PTE, thus reducing its effectiveness against deep-seated tumors. In contrast, the combined nanocatalytic therapy using BCSO NSs plus US and laser irradiation (BCSO + laser + US) demonstrated superior tumor-suppressive outcomes (Supplementary Fig. 51b). Photographs of the right liver lobe tumors from mice on day 13 corroborated these findings, further validating the synergistic action of PTE and sono-piezoelectric catalysis, which outperformed other single treatments. This also highlighted the comparative advantage of sono-piezoelectric catalytic therapy over

https://doi.org/10.1038/s41467-025-61041-4

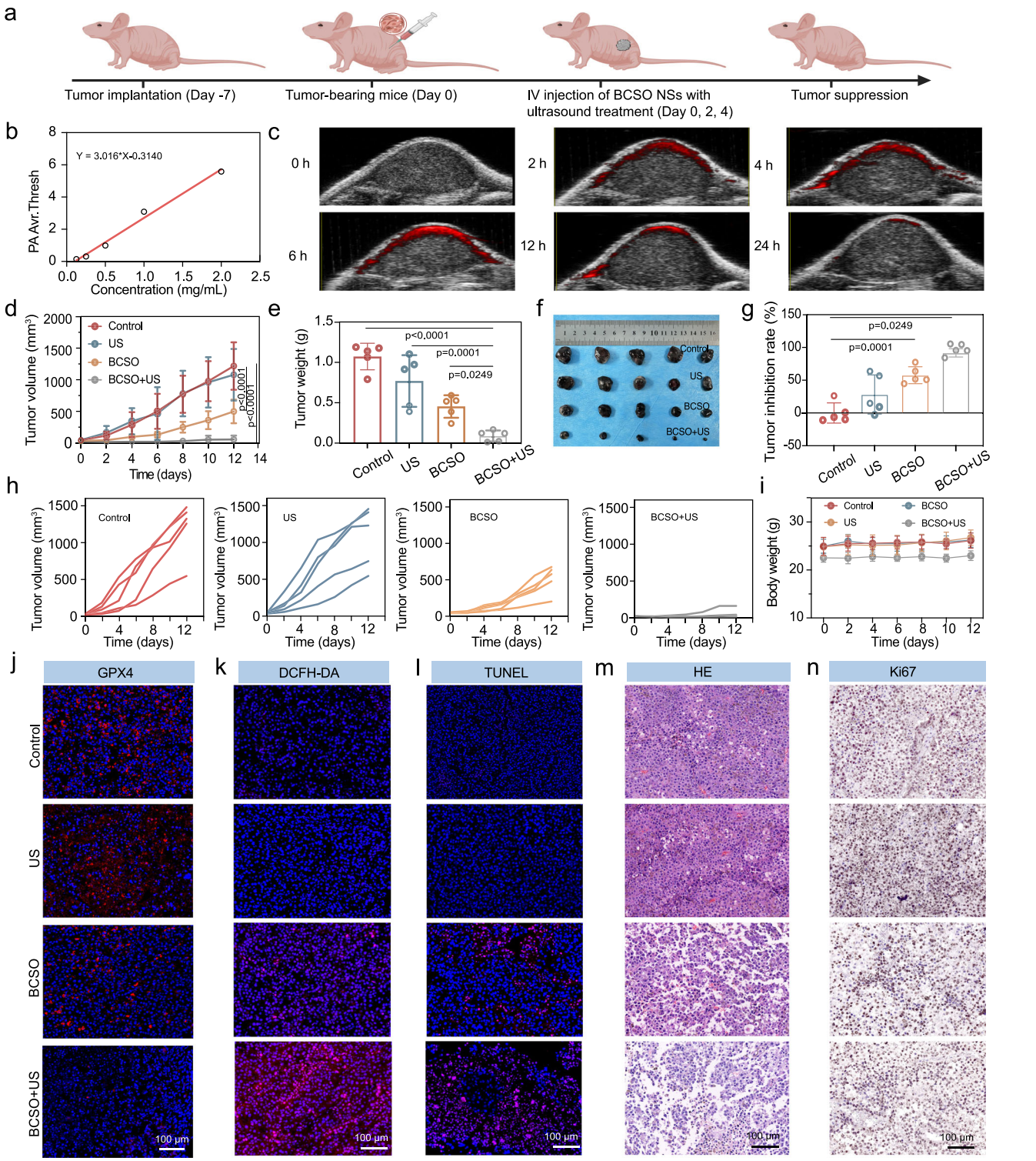

Fig. 9 | In vivo assessment of sono-piezoelectric nanocatalytic antitumor properties. a Experiment illustration of in vivo antitumor therapy (Created with BioRender.com). **b** The corresponding PA signal intensities of BCSO NSs at different concentrations. **c** PA images of tumor site at various time points after intravenous injection of BCSO NSs. **d** Tumor volume in the mice receiving different treatments recorded every 2 days ($n = 5$ mice in each group, mean ± s.d., two-way ANOVA). **e** Tumor weight, (**f**) photographs, (**g**) tumor inhibition rate, (**h**) individual tumor growth curves, and **i** body weight of mice in various groups ($n = 5$ mice in each group, mean ± s.d., one-way ANOVA). **l** TUNEL, (**m**) H&E, and (**n**) ki67 staining of the tumor tissues receiving various treatments. **j** Expression of GPX4 in tumor regions imaged by immunofluorescent staining after different treatments. **k** ROS detection at tumor sites in different treatment groups using DCFH-DA. Source data are provided as a Source Data file.

PTE in combating deeper tumors (Supplementary Fig. 51c)[69]. Meanwhile, the body weight of the mice remained stable throughout the experimental period, suggesting the high biosafety of BCSO NSs. In contrast, the body weight of mice in the control group exhibited a slight increase, likely due to the accumulation of ascites associated with tumor growth (Supplementary Fig. 51d).

H&E and immunohistochemical staining images also showed that the combined treatment was highly effective in suppressing the

proliferation of liver cancer cells (Supplementary Fig. 50e). Additionally, TUNEL staining results revealed significant apoptosis in liver cancer cells treated with synergistic therapy. These results evidence that the enhanced ROS generation by BCSO NSs under the excitation of multiple energy inputs can improve the therapeutic efficacy, thus broadening their potential applications in biomedical fields.

Discussion

ROS are pivotal regulators of redox homeostasis, influencing the development and progression of various pathological conditions. The application of PTE and piezoelectric nanocatalysts in biomedicine presents a significant advancement in ROS-mediated therapeutic strategies. Particularly, constructing heterojunctions offers an effective strategy for combining different catalytic mechanisms to overcome the inadequate ROS yield of bulk nanocatalysts. However, the fabrication of lamellar face-to-face 2D/2D nanostructures remains a formidable challenge. In this work, we developed superlattice BCSO NSs as a multimodal energy transformation nanocatalyst. The natural heterostructures of BCSO NSs render them with exceptional flexibility in leveraging the unique properties of alternatively stacked layers, boosting ROS generation efficiency via multiple catalytic modes. DFT calculations further reveal that BCSO NSs can form an internal electric field within the 2D heterostructures, which facilitates rapid charge separation and inhibits the recombination of generated charge carriers. COMSOL simulations have modeled the potential distribution of BCSO NSs under various external energy inputs. Accordingly, BCSO NSs not only can implement PTE and sono-piezoelectric catalysis under photonic or mechanical energy inputs but also feature notable enzyme-mimicking activities, offering high adaptability for antibacterial and cancer theranostics.

Specifically, the inherent and energy-enhanced enzyme-like catalytic activities of BCSO NSs were validated. The PTE nanocatalytic antibacterial potential of BCSO NSs was demonstrated using a wound infection model. Furthermore, BCSO NSs exhibited remarkable sono-piezoelectric capabilities, enabling the simultaneous generation of $\cdot O_2^-$ and $^1O_2$, along with POD-like activity to produce ·OH and deplete intracellular GSH. This synergistic catalytic action effectively amplifies oxidative stress within melanoma cells, leading to the inactivation of GPX4 and the subsequent accumulation of LPO, ultimately triggering ferroptotic cell death. Notably, in an orthotopic liver cancer model, the combined application of PTE and sono-piezoelectric catalysis resulted in significant tumor suppression, underscoring the therapeutic potential of this dual-modality nanocatalytic approach. This study also elucidates the pivotal role of sono-piezoelectric effects in targeting deep-seated tumors, highlighting the potential of BCSO NSs in addressing complex clinical challenges. By introducing a paradigm of 2D superlattice nanocatalysts, this research expands the scope of nanocatalytic therapies, leveraging multimodal energy conversion for diverse biomedical applications. Moreover, overcoming key challenges related to large-scale production while maintaining structural uniformity and functional integrity will be instrumental in advancing these nanocatalysts toward clinical translation and therapeutic implementation.

Methods

Synthesis of BCSO NSs

To prepare BCSO NSs, 95 mg of $Bi(NO_3)_3{\cdot}5H_2O$ was dissolved in mixture of ultrapure water and ethanol (5 mL each) and stirred for 10 min. Upon forming a milky suspension, 26 mg of selenourea was introduced. This was followed by the stepwise addition of 100 mg PVP (K30), 50 mg $Cu(NO_3)_2{\cdot}3H_2O$, 120 mg KOH, and 320 mg NaOH, with continuous stirring for an additional 15 min to ensure uniform mixing. The resultant black suspension was transferred to a 50 mL Teflon-lined stainless steel autoclave and subjected to hydrothermal synthesis at 180°C for 24 h. After the hydrothermal process, the autoclave was left to cool to room temperature under ambient conditions. The black precipitate was collected via centrifugation (9570 × g, 10 min) and washed twice with both ultrapure water and ethanol to remove unreacted residues. The purified nanosheets were then redispersed in 30 mL of ultrapure water (1 mg mL^{-1}), followed by the addition of 300 µL PEI aqueous solution (20 mg mL^{-1}). The mixture was sonicated for 10 min and stirred at room temperature for an additional hour. The PEI-modified BCSO was subsequently washed twice with ultrapure water. For further modification, 5 mg of PEI-coated BCSO was dispersed in 5 mL DMF, to which 5 mg maleic anhydride and 200 µL triethylamine were added. The reaction was maintained under continuous stirring for 12 h. The resulting product was collected by centrifugation, washed twice with ethanol, and redispersed in ultrapure water for storage and further use.

In vitro evaluation of $^1O_2$ generation

To investigate the production of singlet oxygen ($^1O_2$), BCSO NSs (50 µg mL^{-1}) were mixed with 1 mg mL^{-1} DPBF dissolved in DMF. The mixtures were then subjected to one of the following treatments: thermal cycling (30–45°C, 5 cycles), 1064 nm laser irradiation (1.5 W cm^{-2}, 10 min on/off cycles for 5 cycles), or US exposure (1 MHz, 1 W cm^{-2}, 50% duty cycle) for 5 min. A DPBF-only group served as the control. After treatment, the absorbance was measured in the range of 300–600 nm using a UV–Vis–NIR spectrophotometer. The decline in DPBF's characteristic peak was used to assess the extent of $^1O_2$ generation.

In a complementary assay, ABDA was used as a secondary $^1O_2$ probe. Specifically, 30 µL of 10 mM ABDA (in DMF) was added to 3 mL of BCSO solution (100 µg mL^{-1}), followed by different treatment conditions: (1) thermal cycling (30–45°C, 1 cycle), (2) photothermal cycling (1064 nm laser, 1.5 W cm^{-2}, 1 cycle), (3) US, and (4) combined photothermal cycling and ultrasonic exposure. To establish a temperature gradient, the BCSO NSs dispersed in aqueous solution were alternatively incubated at 30 and 45 °C in a constant temperature oven. The photothermal-induced temperature gradient was generated by irradiating BCSO aqueous suspensions with a 1064 nm laser, with the temperature changes monitored using thermal imaging. Following the treatments, suspensions were centrifuged to remove residual nanosheets. The degradation of ABDA, reflective of $^1O_2$ production, was quantified by recording absorbance spectra from 300 to 450 nm. In addition, ESR spectroscopy was conducted using TEMP as a spin-trapping reagent to further confirm the presence of $^1O_2$.

In vitro evaluation of $\cdot O_2^-$ generation

To assess $\cdot O_2^-$ production, BCSO NSs (50 µg mL^{-1}) were incubated with NBT (1 mg mL^{-1}) dissolved in ethanol. The mixtures were subjected to one of the following treatments: thermal cycling (30–45°C, 10 min on/off, 3 cycles), laser irradiation at 1064 nm (1.5 W cm^{-2}, same cycle conditions), or US exposure (1 MHz, 1 W cm^{-2}, 50% duty cycle). Untreated NBT solution served as the control group. After treatment, the absorbance at 260 nm was recorded using a UV–Vis–NIR spectrophotometer to quantify $\cdot O_2^-$ generation. In addition, ESR spectroscopy was performed using DMPO as a trapping probe to verify the formation of $\cdot O_2^-$.

In vitro evaluation of ·OH generation

The formation of ·OH was evaluated using TMB. 3,3′,5,5′-Tetramethylbenzidine dihydrochloride (TMB·HCl), which was dissolved in ultrapure water to obtain a TMB solution (1 mg mL^{-1}). The TMB solution was mixed with BCSO NSs and H_2O_2 under mildly acidic conditions. When applicable, the mixture was exposed to US irradiation (1 MHz, 1 W cm^{-2}, 50% duty cycle) when necessary. The absorbance of the resulting solution was measured using a UV–Vis–NIR spectrophotometer (500–800 nm), and the absorbance at ~652 nm was used to quantify ·OH production. The effect of pH on ·OH generation was

also systematically evaluated. When applicable, the mixtures were exposed to US irradiation (1 MHz, 1 W cm^{-2}, 50% duty cycle). UV–Vis–NIR spectroscopy (500–800 nm) was used to monitor absorbance changes, with the signal at ~652 nm serving as an indicator of ·OH levels. The influence of pH on ·OH production was also systematically investigated.

To validate the results, MB was employed as a secondary probe. A volume of 30 μL MB solution (1 mg mL^{-1}) was added to mixtures of BCSO NSs and H_2O_2 in acidic media. MB absorbance spectra were collected within 500–800 nm to assess ·OH-mediated degradation. Reactions were performed using varying concentrations of BCSO and H_2O_2, with US exposure applied where indicated. Additionally, ESR analysis was performed using DMPO to capture and confirm the generation of ·OH.

Computational analysis of multimodal catalytic mechanisms

All first-principles calculations were conducted using the Vienna Ab initio Simulation Package (VASP, version 6.1.0) within the framework of DFT and periodic boundary conditions. The projector augmented-wave (PAW) method was employed to describe core–valence interactions, and the exchange–correlation energy was treated using the generalized gradient approximation (GGA) in the Perdew–Burke–Ernzerhof (PBE) formulation. A plane-wave basis set with a kinetic energy cutoff of 500 eV and high-precision settings was employed throughout. Spin-polarized calculations were performed assuming a paramagnetic system. Geometry optimizations were carried out using a Monkhorst–Pack k-point grid of 3×3×1, while a finer grid of 7×7×1 was used for subsequent electronic structure analyses. Convergence thresholds were set at 10^{-5}eV for the total energy and 10^{-4}eVÅ^{-1} for atomic force minimization. Free energy changes (ΔG) for each reduction step were obtained at zero bias were evaluated as

$$\Delta G = \Delta E + \Delta EZPE + T\Delta S \quad (2)$$

where ΔE denotes the total reaction energy, ΔE_{ZPE} represents the zero-point energy correction, T is the absolute temperature, and ΔS refers to the reaction entropy.

Bacterial culture and plate method

E.coli (ATCC 35401) and MRSA (ATCC 43300) were sourced from BeNa Culture Collection Co., Ltd. (Beijing, China). A bacterial suspension with an initial concentration of ~10^9 CFU mL^{-1} was prepared by overnight incubation at 37°C. For the in vitro antibacterial study, the plate method was employed to determine the antibacterial rate using a 12-well plate as the treatment container. Bacterial suspensions were diluted to 10^6 CFU mL^{-1} using sterile water and then treated with BCSO NSs (50 μg mL^{-1}) at 37 °C for 4 h. After treatment, the suspensions were serially diluted and plated on LB agar. Each experimental condition was prepared in triplicate. The plates were incubated at 37°C for 16 h, followed by colony counting to determine bacterial viability. For groups involving laser exposure, including laser-only and BCSO+laser treatments, bacterial suspensions were subjected to 1064 nm laser irradiation (1.5 W cm^{-2}) in an on/off cycle (10 min per cycle, 3 total cycles) prior to plating.

RNA sequencing analysis

MRSA suspensions with a bacterial load of 10^{10} CFU mL^{-1} were exposed to BCSO NSs treatment, followed by three cycles of NIR-II laser irradiation. RNA sequencing was performed by Majorbio (I-Sanger Inc., Shanghai, China). Raw sequencing data were processed and assessed for quality using FASTQ files, Bowtie v1.3.1 for alignment, and RSeQC v2.3.6 for read quality control. DEGs between treatment and control groups were identified using the empirical Bayesian method in the limma R package, with statistical significance defined as an adjusted *P*-value < 0.05. DEG distributions were visualized as volcano plots using ggplot2. Functional annotation of DEGs was performed via GO and KEGG enrichment analyses. The enrichment results were also plotted with ggplot2, and enrichment significance was determined by adjusted $P < 0.05$.

Intracellular ROS evaluation of B16F10 cells

B16F10 cells were seeded in confocal dishes and cultured for 24 h to ensure adherence. The cells were then treated with either culture medium or BCSO NSs (200 μg mL^{-1}) for 12 h. Following treatment, cells were incubated with the ROS-sensitive probe DCFH-DA for 30 min at 37 °C, and subsequently washed twice with PBS to remove excess dye.For the relevant groups, US irradiation (1.0 MHz, 1.0 W cm^{-2}, 50% duty cycle, 5 min) was applied. Cellular fluorescence was then visualized using CLSM, and ROS levels were semi-quantified based on fluorescence intensity using ImageJ software.

Intracellular $\cdot O_2^-$ evaluation of B16F10 cells

B16F10 cells were seeded into confocal dishes and and incubated for 24 h to ensure adhesion. The cells were then incubated with either standard culture medium or BCSO NSs (200 μg mL^{-1}) for 12 h. Afterward, intracellular ROS levels were assessed using the DHE probe. Cells were stained with DHE for 30 min at 37 °C, followed by two PBS washes to eliminate unbound dye. Selected groups were then exposed to US irradiation (1.0 MHz, 1.0 W cm^{-2}, 50% duty cycle, 5 min). The resulting ROS-associated fluorescence was observed using CLSM, and semi-quantitative fluorescence intensity was analyzed using ImageJ software.

Intracellular GSH depletion assay

B16F10 cells were cultured in confocal dishes and subjected to four treatment groups: Control, US, BCSO NSs, and BCSO + US. After treatment, cells were incubated with Thiol Tracker Violet (10 μM) for 30 min at 37 °C. Subsequently, cells were rinsed twice with PBS and observed under CLSM. The intracellular fluorescence intensity was analyzed using ImageJ to evaluate GSH depletion.

In parallel, similarly treated cells were harvested for quantitative determination of intracellular GSH levels using a commercial detection kit, following the manufacturer's instructions. The assay was used to compare GSH content among the groups.

Intracellular LPO level assessment

B16F10 cells were seeded into confocal culture dishes and incubated overnight to allow adherence. Once the cell confluency reached ~80%, they were divided into four groups for treatment: Control, US, BCSO NSs, and BCSO + US. After completing the respective treatments, cells were rinsed three times with PBS to remove residual agents. To evaluate intracellular LPO, cells were incubated with the LPO-sensitive fluorescent probe C11-BODIPY$^{581/591}$ (10 μM) for 30 min at 37 °C. Following staining, cells were washed again with PBS to remove unbound dye, and intracellular fluorescence signals were visualized using CLSM.

Statistics and reproducibility

All experiments were independently repeated at least three times with similar results. Representative experiments shown (e.g., micrographs, colony images) were independently repeated three times, yielding similar results. In the Fig. legends, n indicates either the number of independent samples or the number of mice used. Data are expressed as mean ± SD. For multiple group comparisons, One-way and Two-way ANOVA were conducted. A *P*-value < 0.05 was considered to indicate statistical significance. Statistics analysis were performed with GraphPad Prism 10.2.0 software.

Animal experiments

All animal experiments were performed with the approval of the Ethics Committee of Shanghai University (License number: ECSHU-2021-

029). All mice were kept in accordance with the policies on animal research of the National Ministry of Health. Male ICR mice (6–8 weeks old) were chosen for in vivo biosafety evaluation and wound healing model establishment. Male Balb/c nude mice (6–8 weeks old) were chosen for establishing a B16F10 tumor-bearing mouse model. Furthermore, female Balb/c nude mice (6–8 weeks old) were chosen to establish an orthotopic H22 liver cancer mode. And the sex of the mice does not affect the results of the experiments. 1500 mm^3 was set as the permitted maximal tumor size in conventional in vivo antitumor experiments and this limit was not exceeded during the course of the study. Mice were acclimatized for 7 days in an SPF facility (12 h light/dark, 22 °C, 50% humidity) prior to experiments. Bedding, food, and water were sterilized to maintain SPF status.

Reporting summary

Further information on research design is available in the Nature Portfolio Reporting Summary linked to this article.

Data availability

All data underlying this study are available from the corresponding author upon request. The authors declare that all data needed to support the findings of this study are provided within the article, Supplementary information, and Source data file. The raw data of RNA-sequencing has been deposited in the National Center for Biotechnology Information (BioProject accession number PRJNA1252678: https://www.ncbi.nlm.nih.gov/sra/?term=PRJNA1252678). Source data are provided as a Source Data file. Source data are provided with this paper.

References

1. Gong, N. et al. Carbon-dot-supported atomically dispersed gold as a mitochondrial oxidative stress amplifier for cancer treatment. *Nat. Nanotechnol.* **14**, 379–387 (2019).
2. Hu, X. et al. An artificial metabzyme for tumour-cell-specific metabolic therapy. *Nat. Nanotechnol.* **19**, 1712–1722 (2024).
3. Sancho-Albero, M. et al. Cancer-derived exosomes loaded with ultrathin palladium nanosheets for targeted bioorthogonal catalysis. *Nat. Catal.* **2**, 864–872 (2019).
4. Lin, H., Chen, Y. & Shi, J. Nanoparticle-triggered in situ catalytic chemical reactions for tumour-specific therapy. *Chem. Soc. Rev.* **47**, 1938–1958 (2018).
5. Tang, Z., Zhao, P., Wang, H., Liu, Y. & Bu, W. Biomedicine meets fenton chemistry. *Chem. Rev.* **121**, 1981–2019 (2021).
6. Sun, M. et al. Single-atom catalysts mediated bioorthogonal modulation of N_6-methyladenosine methylation for boosting cancer immunotherapy. *J. Am. Chem. Soc.* **146**, 8216–8227 (2024).
7. Mao, C. et al. Delivery of an ectonucleotidase inhibitor with ROS-responsive nanoparticles overcomes adenosine-mediated cancer immunosuppression. *Sci. Transl. Med.* **14**, eabh1261 (2022).
8. Glorieux, C., Liu, S., Trachootham, D. & Huang, P. Targeting ROS in cancer: rationale and strategies. *Nat. Rev. Drug. Discov.* **23**, 583–606 (2024).
9. Huo, M., Wang, L., Chen, Y. & Shi, J. Tumor-selective catalytic nanomedicine by nanocatalyst delivery. *Nat. Commun.* **8**, 357 (2017).
10. Zhao, B. et al. Photocatalysis-mediated drug-free sustainable cancer therapy using nanocatalyst. *Nat. Commun.* **12**, 1345 (2021).
11. Huo, M. et al. Magnesium hexacyanoferrate nanocatalysts attenuate chemodrug-induced cardiotoxicity through an anti-apoptosis mechanism driven by modulation of ferrous iron. *Nat. Commun.* **13**, 7778 (2022).
12. Wang, M. et al. Tumor-microenvironment-activated reactive oxygen species amplifier for enzymatic cascade cancer starvation/chemodynamic/immunotherapy. *Adv. Mater.* **34**, e2106010 (2022).
13. Li, Y. et al. Tumour-microenvironment-responsive $Na_2S_2O_8$ nanocrystals encapsulated in hollow organosilica-metal-phenolic networks for cycling persistent tumour-dynamic therapy. *Exploration (Beijing)* **4**, 20230054 (2024).
14. Liu, J. et al. A titanium nitride nanozyme for pH-responsive and irradiation-enhanced cascade-catalytic tumor therapy. *Angew. Chem. Int. Ed.* **60**, 25328–25338 (2021).
15. Zhang, M. et al. Two-dimensional MXene-originated in situ nanosonosensitizer generation for augmented and synergistic sonodynamic tumor nanotherapy. *ACS Nano* **16**, 9938–9952 (2022).
16. Kang, Y. et al. A novel cascaded energy conversion system inducing efficient and precise cancer therapy. *Bioact. Mater.* **20**, 663–676 (2023).
17. Jiang, X. et al. A photo-activated thermoelectric catalyst for ferroptosis-/pyroptosis-boosted tumor nanotherapy. *Adv. Healthc. Mater.* **12**, e2300699 (2023).
18. Wang, Y. et al. Piezo-catalysis for nondestructive tooth whitening. *Nat. Commun.* **11**, 1328 (2020).
19. Xu, Q. et al. Construction of bio-piezoelectric platforms: from structures and synthesis to applications. *Adv. Mater.* **33**, e2008452 (2021).
20. Fan, Y. et al. Biomimetic piezoelectric nanomaterial-modified oral microrobots for targeted catalytic and immunotherapy of colorectal cancer. *Sci. Adv.* **10**, eadm9561 (2024).
21. Chen, S. et al. Piezocatalytic medicine: an emerging frontier using piezoelectric materials for biomedical applications. *Adv. Mater.* **35**, e2208256 (2023).
22. Zang, P. et al. Phase engineered Cu_xS-Ag_2S with photothermoelectric activity for enhanced multienzyme activity and dynamic therapy. *Adv. Mater.* **36**, e2400416 (2024).
23. Zang, P. Y. et al. Photothermal-actuated thermoelectric therapy by harnessing janus-structured Ag-AgS nanoparticles with enhanced antitumor efficacy. *Chem. Mater.* **35**, 7770–7780 (2023).
24. Ma, M. et al. Coupling pyroelectric fields and donor doping to adjust Curie temperature and band structure to access to highly efficient $BaTiO_3$ photoelectrodes for dye degradation. *Appl. Surf. Sci.* **682**, 161779 (2025).
25. Zhu, Y. et al. Thermoelectric nanoheterojunction-mediated multiple energy conversion for enhanced cancer therapy. *ACS Nano* **18**, 34257–34271 (2024).
26. Zhang, L. et al. A narrow-bandgap RuI_3 nanoplatform to synergize radiotherapy, photothermal therapy, and thermoelectric dynamic therapy for tumor eradication. *Acta Biomater.* **182**, 188–198 (2024).
27. Yuan, X. et al. Self-triggered thermoelectric nanoheterojunction for cancer catalytic and immunotherapy. *Nat. Commun.* **14**, 5140 (2023).
28. Huang, H. et al. Mitochondria-specific nanocatalysts for chemotherapy-augmented sequential chemoreactive tumor therapy. *Exploration* **1**, 50–60 (2021).
29. You, H. et al. Accelerated pyro-catalytic hydrogen production enabled by plasmonic local heating of Au on pyroelectric $BaTiO_3$ nanoparticles. *Nat. Commun.* **13**, 6144 (2022).
30. Zhu, P., Chen, Y. & Shi, J. Piezocatalytic tumor therapy by ultrasound-triggered and $BaTiO_3$-mediated piezoelectricity. *Adv. Mater.* **32**, e2001976 (2020).
31. Zhang, S. et al. Nanoheterojunction engineering enables nir-ii-triggered photonic hyperthermia and pyroelectric catalysis for tumor-synergistic therapy. *Adv. Funct. Mater.* **33**, 2302360 (2023).
32. Min, M. et al. Photothermally enabled pyro-catalysis of a $BaTiO_3$ nanoparticle composite membrane at the liquid/air interface. *ACS Appl. Mater. Interfaces* **10**, 21246–21253 (2018).
33. Ahmad, I. et al. Recent advances and challenges in 2D/2D heterojunction photocatalysts for solar fuels applications. *Adv. Colloid Interface Sci.* **304**, 102661 (2022).
34. Shifa, T. A., Wang, F., Liu, Y. & He, J. Heterostructures based on 2D materials: a versatile platform for efficient catalysis. *Adv. Mater.* **31**, e1804828 (2019).

35. Kwon, N. H. et al. Monolayered g-C_3N_4 nanosheet as an emerging cationic building block for bifunctional 2D superlattice hybrid catalysts with controlled defect structures. *Appl. Catal. B.* **277**, 119191 (2020).
36. Zhao, B. et al. High-order superlattices by rolling up van der Waals heterostructures. *Nature* **591**, 385–390 (2021).
37. Zhao, L. D. et al. BiCuSeO oxyselenides: firest promising thermoelectric materials. *Energy Environ. Sci.* **7**, 2900–2924 (2014).
38. Ren, G. K. et al. Complex electronic structure and compositing effect in high performance thermoelectric BiCuSeO. *Nat. Commun.* **10**, 2814 (2019).
39. Li, J. et al. Chemical vapor deposition of quaternary 2D BiCuSeO p-type semiconductor with intrinsic degeneracy. *Adv. Mater.* **34**, 2207796 (2022).
40. Tang, W. et al. BiCuSeO based thermoelectric materials: Innovations and challenges. *Mater. Today Phys.* **35**, 101104 (2023).
41. Li, F. et al. Polycrystalline BiCuSeO oxide as a potential thermoelectric material. *Energy Environ. Sci.* **5**, 7188–7195 (2012).
42. Taifan, W., Boily, J.-F. & Baltrusaitis, J. Surface chemistry of carbon dioxide revisited. *Surf. Sci. Rep.* **71**, 595–671 (2016).
43. Burghaus, U. Surface chemistry of CO_2 – Adsorption of carbon dioxide on clean surfaces at ultrahigh vacuum. *Prog. Surf. Sci.* **89**, 161–217 (2014).
44. Cheng, J. Y. et al. Piezocatalytic schottky junction treats atherosclerosis by a biomimetic trojan horse strategy. *Adv. Mater.* **36**, 2312102 (2024).
45. Chen, L. et al. Edge modification facilitated heterogenization and exfoliation of two-dimensional nanomaterials for cancer catalytic therapy. *Sci. Adv.* **8**, eabo7372 (2022).
46. You, H. et al. Harvesting the vibration energy of $BiFeO_3$ nanosheets for hydrogen evolution. *Angew. Chem. Int. Ed.* **58**, 11779–11784 (2019).
47. Hu, C. et al. Coupling piezocatalysis and photocatalysis in Bi_4NbO_8X (X = Cl, Br) polar single crystals. *Adv. Funct. Mater.* **30**, 1908168 (2020).
48. Dong, Y. et al. 2D Piezoelectric Bi_2MoO_6 nanoribbons for GSH-enhanced sonodynamic therapy. *Adv. Mater.* **33**, e2106838 (2021).
49. Truong Hoang, Q. et al. Piezocatalytic 2D WS_2 nanosheets for ultrasound-triggered and mitochondria-targeted piezodynamic cancer therapy synergized with energy metabolism-targeted chemotherapy. *Adv. Mater.* **35**, e2300437 (2023).
50. Wang, K. et al. The mechanism of piezocatalysis: energy band theory or screening charge effect? *Angew. Chem. Int. Ed.* **61**, e202110429 (2022).
51. Wang, S. Y. et al. Reduced graphene oxides modified Bi_2Te_3 nanosheets for rapid photo-thermoelectric catalytic therapy of bacteria-infected wounds. *Adv. Funct. Mater.* **33**, 2210098 (2023).
52. Zong, L. et al. Oxygen-vacancy-rich molybdenum carbide MXene nanonetworks for ultrasound-triggered and capturing-enhanced sonocatalytic bacteria eradication. *Biomaterials* **296**, 122074 (2023).
53. Jiang, P. et al. Tuning oxidant and antioxidant activities of ceria by anchoring copper single-site for antibacterial application. *Nat. Commun.* **15**, 1010 (2024).
54. Chang, M. et al. Ultrasound-amplified enzyodynamic tumor therapy by perovskite nanoenzyme-enabled cell pyroptosis and cascade catalysis. *Adv. Mater.* **35**, e2208817 (2023).
55. Gong, F. et al. Ultrasmall oxygen-deficient bimetallic oxide MnWOx nanoparticles for depletion of endogenous gsh and enhanced sonodynamic cancer therapy. *Adv. Mater.* **31**, 1900730 (2019).
56. Setiawan, S. A. et al. Synergistic disruption of BTK and BCL-2 causes apoptosis while inducing ferroptosis in double-hit lymphoma. *Eur. J. Pharmacol.* **943**, 175526 (2023).
57. Lee, Y. S. et al. BAX-dependent mitochondrial pathway mediates the crosstalk between ferroptosis and apoptosis. *Apoptosis* **25**, 625–631 (2020).
58. Gitego, N. et al. Chemical modulation of cytosolic BAX homodimer potentiates BAX activation and apoptosis. *Nat. Commun.* **14**, 8381 (2023).
59. Lopez, A. et al. Co-targeting of BAX and BCL-XL proteins broadly overcomes resistance to apoptosis in cancer. *Nat. Commun.* **13**, 1199 (2022).
60. Bloch, N. B. et al. The conformational stability of pro-apoptotic BAX is dictated by discrete residues of the protein core. *Nat. Commun.* **12**, 4932 (2021).
61. Du, Y. Q. et al. A vacancy-engineering ferroelectric nanomedicine for cuproptosis/apoptosis co-activated immunotherapy. *Adv. Mater.* **36**, 2403253 (2024).
62. Hou, D. Y. et al. In vivo assembly enhanced binding effect augments tumor specific ferroptosis therapy. *Nat. Commun.* **15**, 454 (2024).
63. Tian, B. et al. Doping engineering to modulate lattice and electronic structure for enhanced piezocatalytic therapy and ferroptosis. *Adv. Mater.* **35**, e2304262 (2023).
64. Xiong, T. et al. Lipid droplet targeting type I photosensitizer for ferroptosis via lipid peroxidation accumulation. *Adv. Mater.* **36**, e2309711 (2024).
65. Cao, Y. et al. An intelligent nanoplatform for orthotopic glioblastoma therapy by nonferrous ferroptosis. *Adv. Funct. Mater.* **32**, 2209227 (2022).
66. He, Y.-J. et al. Fenton reaction-independent ferroptosis therapy via glutathione and iron redox couple sequentially triggered lipid peroxide generator. *Biomaterials* **241**, 119911 (2020).
67. Wang, Y. et al. Remodeling tumor-associated neutrophils to enhance dendritic cell-based HCC neoantigen nano-vaccine efficiency. *Adv. Sci.* **9**, e2105631 (2022).
68. Li, Z. et al. Combined anti-hepatocellular carcinoma therapy inhibit drug-resistance and metastasis via targeting "substance P-hepatic stellate cells-hepatocellular carcinoma" axis. *Biomaterials* **276**, 121003 (2021).
69. Deng, Y. et al. Tailoring supramolecular prodrug nanoassemblies for reactive nitrogen species-potentiated chemotherapy of liver cancer. *ACS Nano.* **15**, 8663–8675 (2021).

Acknowledgements

This work is financially supported by National Key Research and Development Projects (Grants No. 2023YFC2306500), National Natural Science Foundation of China (Grant No. 52102350, 82202190, 82071928), Program of Shanghai Academic/Technology Research Leader (Grant No. 23XD1401300), Chenguang Program of the Shanghai Education Development Foundation and Shanghai Municipal Education Commission, Shanghai Science and Technology Program (Grants No. 21010500100 and 24520712900), Shuguang Program supported by Shanghai Education Development Foundation and Shanghai Municipal Education Commission (Grants No. 21SG39), and Animal Research Program from Science and Technology Commission of Shanghai Municipality (Grants No. 22140901700). The authors also thank home-for-researchers for their help in the preparation of the schematic diagram.

Author contributions

L. C., S. Z., J. Z. and Y. C. conceived and designed the experiments. S. Z., X. K. and W. X. performed experiments. S. Z., X. X. and Q. H. contributed to the analysis and interpretation of the results and the writing of the manuscript. W. X., L. C., J. Z. and Y. C. secured funding. Everyone reviewed and approved the manuscript.

Competing interests

The authors declare no competing interests.

Additional information

Supplementary information The online version contains supplementary material available at https://doi.org/10.1038/s41467-025-61041-4.

Correspondence and requests for materials should be addressed to Liang Chen, Jianqiao Zhou or Yu Chen.

Peer review information *Nature Communications* thanks Mohammad Ruhul Amin Bhuiyan, Guang-Kun Ren, XianZeng Zhang and the other, anonymous, reviewer(s) for their contribution to the peer review of this work. A peer review file is available.